EFFECT OF ADDING PALM FIBER TO THERMAL CONDUCTIVITY OF QUICK SET CONCRETE

A Thesis

by

MONICA GARCIA

Submitted to the Graduate College of
The University of Texas Rio Grande Valley
In partial fulfillment of the requirements for the degree of

MASTER OF SCIENCE IN ENGINEERING

December 2020

Major Subject: Mechanical Engineering

EFFECT OF ADDING PALM FIBER TO THERMAL CONDUCTIVITY OF QUICK SET CONCRETE

A Thesis
by
MONICA GARCIA

COMMITTEE MEMBERS

Dr. Maysam Pournik
Chair of Committee

Dr. Jongmin Kim
Chair of Committee

Dr. Philip Park
Committee Member

Dr. Horacio Vasquez
Committee Member

Dr. Constantine Tarawneh
Committee Member

December 2020

ABSTRACT

Garcia, Monica I., Effect of Adding Palm Fiber to Thermal Conductivity of Quick Set Concrete. Master of Science in Engineering (MSE), December 2020, 86 pp., 36 tables, 25 figures, 54 references.

As climate change becomes a more dire issue accepted by those in power, the demand for local and systemic solutions grows louder. One concern is the contribution of anthropogenic heat from buildings to localized warming of the environment. A method that can reduce anthropogenic heat is decreasing the thermal conductivity of building materials. The objective of this study is to examine the use of palm fibers to reduce the thermal conductivity of quick-set concrete samples. The data gathered in this study are used to determine the thermal conductivity value of samples with varying weight percentages of palm fiber. These results lend evidence to the worth of exploring the use of local sources of organic fibers to reduce the thermal conductivity of building materials which may reduce anthropogenic heat from building constructions. Based on the results of this study, adding palm fiber reduces the thermal conductivity of quick-set concrete samples.

DEDICATION

I would like to dedicate this thesis to my family. My parents, Ricardo and Patricia Garcia for their endless love, support, and part-time editing and reading of my manuscripts. I would also like to dedicate this thesis to my sister Dr. Elysia Garcia for both commiserating with me about the research process and her advice on statistical analysis that likely looks infantile to her Ph.D. level of expertise.

ACKNOWLEDGMENTS

I would like to thank Dr. Pournik and Dr. Kim for their endless encouragement and advice as my thesis committee co-chairs. This thesis would not have been possible without both of your efforts as my mentors. From helping me obtain lab access to commenting and recommending changes to this manuscript. Thank you again for the opportunity to give presentations, research, and contribute to the university.

To Dr. Park, thank you for your aid and expertise in concrete construction. Your guidance made completing this study possible.

To Mirza, thank you for helping a mechanical engineer by making samples in your department's lab.

To Professor Sanchez, thank you for your endless help and patience in the materials lab while I experimented with methods to construct test samples and later aiding with finishing them for testing. This study would've been much more difficult without your help.

To the Office for Sustainability, thank you for the great opportunity to do data collection and analysis for the benefit of the university.

To Dr. Grewal, thank you for giving me the opportunity to study under the Presidential Graduate Research Assistantship grant and contribute to the university.

TABLE OF CONTENTS

LIST OF TABLES

Page

LIST OF FIGURES

Page

LIST OF EQUATIONS

Page

CHAPTER I

BACKGROUND AND INTRODUCTION

Building materials can impact the energy efficiency of a building as well as the temperature of the surrounding area. This unique problem of metropolitan areas recording higher temperatures than nearby rural areas is defined by the Environmental Protection Agency (EPA) as the urban heat island (UHI) effect. Some negative effects of UHI are increases in summertime peak energy demand, air pollution, greenhouse gas emissions, heat-related illnesses, and water pollution. In addition to these environmental impacts, UHI can also affect the health of the populations living in these UHI-touched areas. These include but are not limited to increased respiratory issues, heat stroke, and even heat-related deaths. According to the Centers for Disease Control and Prevention, from 1979–2003, it is estimated that excessive heat exposure contributed to more than 8,000 premature deaths in the United States (Environmental Protection Agency, 2019). While the EPA doesn't quantify the effect of UHI on heat-related illnesses and death, they do emphasize that UHI will exacerbate naturally occurring heat waves which will in turn likely cause more heat-related casualties (Environmental Protection Agency, 2019).

One factor that contributes to UHI is anthropogenic heat from constructions made from materials with higher thermal conductivity values. According to Kandya and Mohan, although the use of the construction materials with low thermal conductivity does not directly mitigate the UHI effect, the improved insulation may reduce the energy and heat for cooling down the

buildings thereby mitigating the UHI effect (Kandya & Mohan, 2018) . Some research has focused on efforts such as added sun shading and recovering heat from the building as effective methods to ease contributions to UHI (Magli et al., 2015). Other research has focused on creating or modifying existing construction materials to increase their thermal resistivity values to minimize anthropogenic heat from buildings made from these materials (Abolarin, et al., 2013). However, some of this research was conducted through computer-generated modeling that analyzed the effect of changing the building envelope to varying materials and thicknesses (Kandya & Mohan, 2018). Other research used modeling to determine the possible effect of changing the roofs of the building in addition to more insulation to the building's envelope (Magli et al., 2015). While such research is necessary and beneficial to the field's collective knowledge, it is also imperative to study experimental materials/composites outside of thermal modeling such as studies done by Elfordy measuring the thermal and mechanical properties of lime and hemp fiber concrete (Elfordy et al., 2008). The goal of this study was to test the hypothesis that adding palm fiber reduces the thermal conductivity of quick-set concrete. Also, compression tests were done on the samples.

1.1 Defining Thermal Conductivity

By understanding the properties of the most popular building materials, selections can be made to reduce energy expenditures. Thus, the study of building materials' thermal conductivity can impact the energy efficiency of the building, and its effect in elevating the temperature of its surrounding areas. Thermal conductivity (*k*), or capability of conducting heat, is defined as "the quantity of heat that passes in unit time through a unit area of a plate whose thickness is unity when its opposite faces differ in temperature by one degree" the units for *k* are watts per meter Kelvin, $k = \frac{W}{m*K}$ (Merriam-Webster, n.d.). To state more plainly, thermal conductivity can be

described as how easily a material can conduct heat like how materials can conduct electricity such as copper. Consequently, metals tend to have high *k* values and conduct heat well while materials like Styrofoam and insulation require more energy to heat the other side of the material. This literature review will look at how differently made brick can impact the building's thermal conductivity. Also, the properties of experimental brick applications and their impact on the heat island effect will provide context for the desired topic for this thesis.

1.1.1 Urban Heat Island Effect and Impact

As urbanization and sprawl increase, there is an increase in the presence of manufactured materials that tend to have greater heat storage capacity as well as lower reflectivity of solar radiation. Therefore, these buildings can become sources of thermal radiation. This is supported by research from He, who summarizes the energy balance equation of UHI formation as the following Equation 3 (He, 2019).

Equation 1 – UHI formation energy balance equation (He, 2019)

$$Q^* + Q_F = Q_H + Q_E + Q_S + \Delta Q_A$$

Where;

- Where Q^* represents solar radiation
- Q_F is heat generated during anthropogenic activities;
- Q_H represents turbulent sensible heat-flux;
- Q_E is dissipated heat via evaporation and transpiration;
- Q_S the heat stored in building or road systems;
- ΔQ_A is net horizontal heat transferred into other systems.

He also notes that while the incoming energy from the sun cannot be modified, modifying the anthropogenic heat loss can be done as HVAC operation is a determinant on the impact of UHI (He, 2019).

Furthermore, a decrease in native vegetation can contribute to an increased heat island effect since they can help keep the surface up to 20°C cooler than pavement (Streutker, 2003). Because of these separate issues, the localized temperatures of urban environments increase. The author continues by stating that the easier way to regulate the temperature of pavement is to change its reflectivity. However, porous pavements without water retention properties tend to be hotter during the day due to their course structure and be cooler at night due to their lower thermal inertia. This phenomenon is the basis for a study conducted by researchers at Rice University.

1.1.2 Study of Urban Heat Island Effect in Houston Texas and surrounding areas

David Streutker of Rice University researched the change of the surface temperature from UHI in Houston, Texas by comparing two sets of measurements 12 years apart. Historical temperature data of local rural areas were used as a reference. The study utilized Advanced Very High-Resolution Radiometers (NOAA, Washington DC) aboard the NOAA polar-orbiting satellites (NOAA, Washington DC). The city had grown by 20% between 1990 and 2000 from 1.63 million to 1.95 million people. Houston's minimal zoning laws led to vast sprawl with a total area of about 1400 km^2 and a lower population density. Data collection consisted of 82 images of Houston on clear cloud-free days from March 1985 through February 1987 (interval 1) and 125 images of the city on clear days from July 1999 through June 2001 (interval 2).

The heat island effect was obtained using the following three equations for Gaussian surface:

Equation 2 - Equations utilized by Dr. Streutker to obtain Gaussian Surface (summarized)

$$T_i(R_i) = \frac{C_2 \nu_j}{\ln\left(1 + \frac{C_1 \nu^3}{R_i}\right)}$$

$$T_{surface} = T_{4(channel\ 4)} + R(T_{4(channel\ 4)} - T_{5(channel\ 5)})$$

$$T(x,y) = T_o + a1x + a2x + ao * \exp\left[-\frac{((x-xo)cos\varphi + (y-yo)\sin\varphi)^2}{.5a_y^2}\right]$$

The mean rural temperatures 10 years apart (17.2 ± .7 °C and 17.1 ± .8°C) were almost the same close enough that there appeared to be no significant difference in the area in the different two-year intervals, Dr. Streutker deemed that the instruments were well-calibrated to each other (Streutker, 2003). When looking at the mean UHI magnitude of Houston (the value a_o from the equations above) for interval 1 was 2.37 ± .07 K, and for interval 2 was .82 ± .1 K. Figure 1 depicts a normalized histogram of the UHI magnitudes. The dashed line shows the UHI magnitudes from interval 1, while the solid line shows the UHI magnitudes from interval 2.

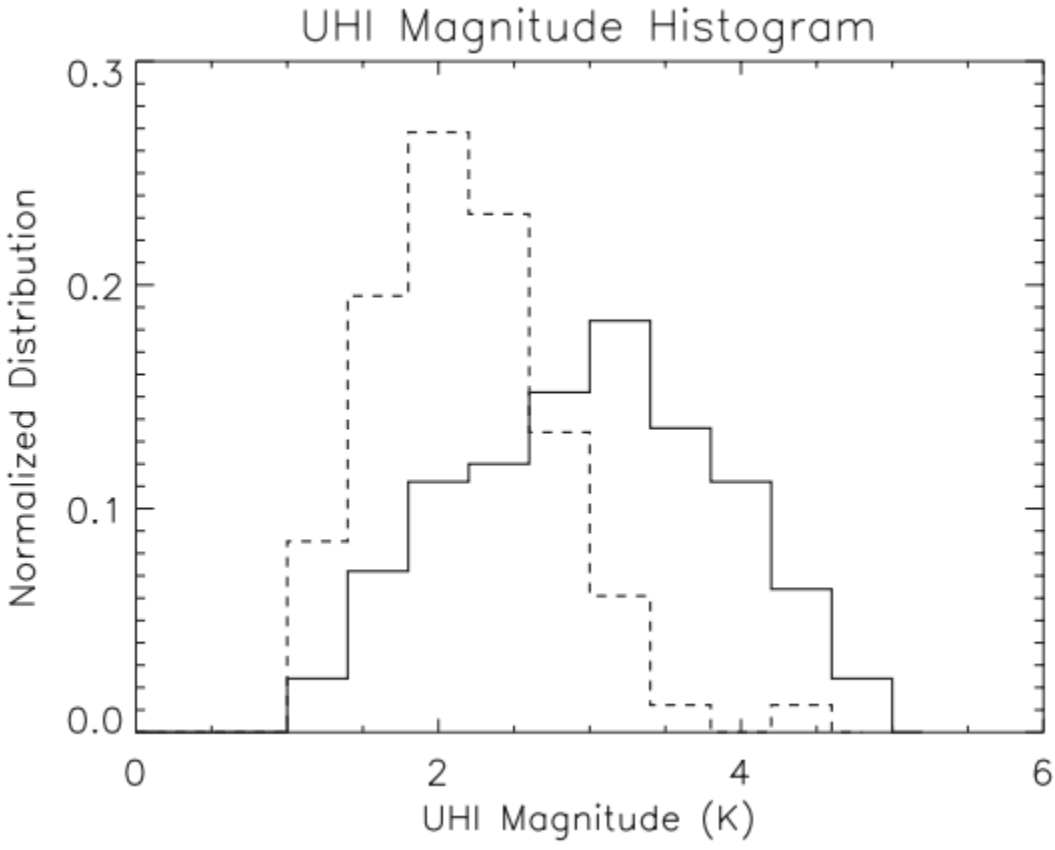

Figure 1 - UHI Magnitude of Houston Histogram (Streutker, 2003)

The Interval 1 data distribution (depicted with a dashed line) peaks at around 2 K compared to the Interval 2 peak at about 3.5 K. This result shows that the magnitude of the UHI

for Houston increased in the twelve years between the end of Interval 1's data collection and the start of Interval 2's data collection. Also, the change in distribution supports that increased urbanization can increase the effect of an urban heat island.

In addition, the study found that as the population increased by 20 % (300,000 residents between 1990 to 2000) so did the scale as the heat island along with its magnitude (about 30%). They found that between 1987 to 1999 the mean nighttime surface temperature heat island increased .82 ±.10 K in magnitude with a growth in the mean area of the UHI between 170 to 650 km^2 (Streutker, 2003).

1.1.3 Urban Heat Island Effect Mitigations

Reducing the thermal conductivity of building material, it must be emphasized, should not be considered the sole method of reducing heat loss and energy consumption. But as, Anurag Kandya cites in their article, *Mitigating the Urban Heat Island Effect through Building Envelope Modifications*, less anthropogenic heat from buildings made of materials with high thermal resistivity can help mitigate the urban heat island effect (Kandya & Mohan, 2018).

While there is research on the harms that UHI can cause, there is also research on mitigations that can be undertaken by metropolitan areas. Mohajerani et al. (2017) highlighted common efforts such as sun shading, building heat recovery, and minimization of heat loss as effective mitigations against UHI in metropolitan areas. Kandra and Mahan (2018) analyzed the thermal performance of alternative materials like bamcrete (a bamboo-concrete composite) and rammed earth in addition to conventional materials (brick and concrete) as methods to reduce heat loss specifically. They incorporated these materials to analyze the effect of building envelope modifications such as increasing the wall thickness and introducing wall cavities.

1.1.4 Discussion of Mitigating Urban Heat Island Effect via Building Envelope Modifications

Kandya and Mahan generated a simulation of the building's hourly energy consumption using software called "eQuest". For the simulation, real data including building dimensions, existing footprint data, and weather data of a four-story university building were incorporated. The researchers created six cases of different wall materials for the computer simulation and the benefits of each case were determined (Table 1).

Table 1 - Different wall materials and their composite thermal resistance

Scenarios	Wall material	Specifications	Composite thermal resistance (R) (m^2 K/W)
Base case	Brick wall	4 in. brick wall with 1 in. plaster	.20
Scenario – 1	Brick wall	8 in. brick wall with 1 in. plaster	.35
Scenario – 2	Brick wall	12 in. brick wall with 1 in. plaster	.49
Scenario – 3	Brick cavity wall	8 in. brick wall with 1 in. cavity and 1 in. plaster	.63
Scenario – 4	Rammed earth	11.8 in. rammed earth with 1 in. plaster	.62
Scenario – 5	Bamboo-concrete composite	2 in. full bamboo with 1 in. concrete and 1 in plaster	.47
Scenario – 6	Bamboo-concrete composite	Double layer 2 in. full bamboo with 1 in. concrete and 1 in plaster	.70

The article referencing data set of summers in 2008 and 2009 found the single-layer brick wall (base case) showed the highest energy use for cooling among all 7 cases. In contrast, scenario 1 reduced energy consumption by 4.2–4.6% for the summer and of 4.7–5.3% annually

during 2008–2009. In addition to improved performance, scenario 3's construction has an additional benefit of sound insulation and it can be attractive in a louder urban environment. The rammed earth scenario 4 may be a good option in certain cases due to the larger thickness of the material (300 mm) in addition to utilizing locally available materials like sand, silt, clay, and gravel. While scenario 4 performs marginally better than scenario 3, rammed earth is a less energy-intensive material than a brick to manufacture as it compacts damp soil and other aggregates in temporary forms (Figure 2). Scenario 5 is particularly intriguing since it consisted of a 2 in. bamboo layer sandwiched between .5 in concrete with a .5 in plaster finish on both sides (4 in. total) and achieved a 3.0-4.5% summer consumption reduction and a 3.4-4.9% annual reduction compared to the base case. This is encouraging as scenarios 1 through 3 had required increasing the thickness of the wall to achieve positive results while scenario 5 reduced its thickness by an inch compared to the base case. Scenario 6 had the overall best performance of the modified cases, compared to the base case as it reduced summer consumption by 6.7-6.8%

and annual cooling by 7.3-7.5%.

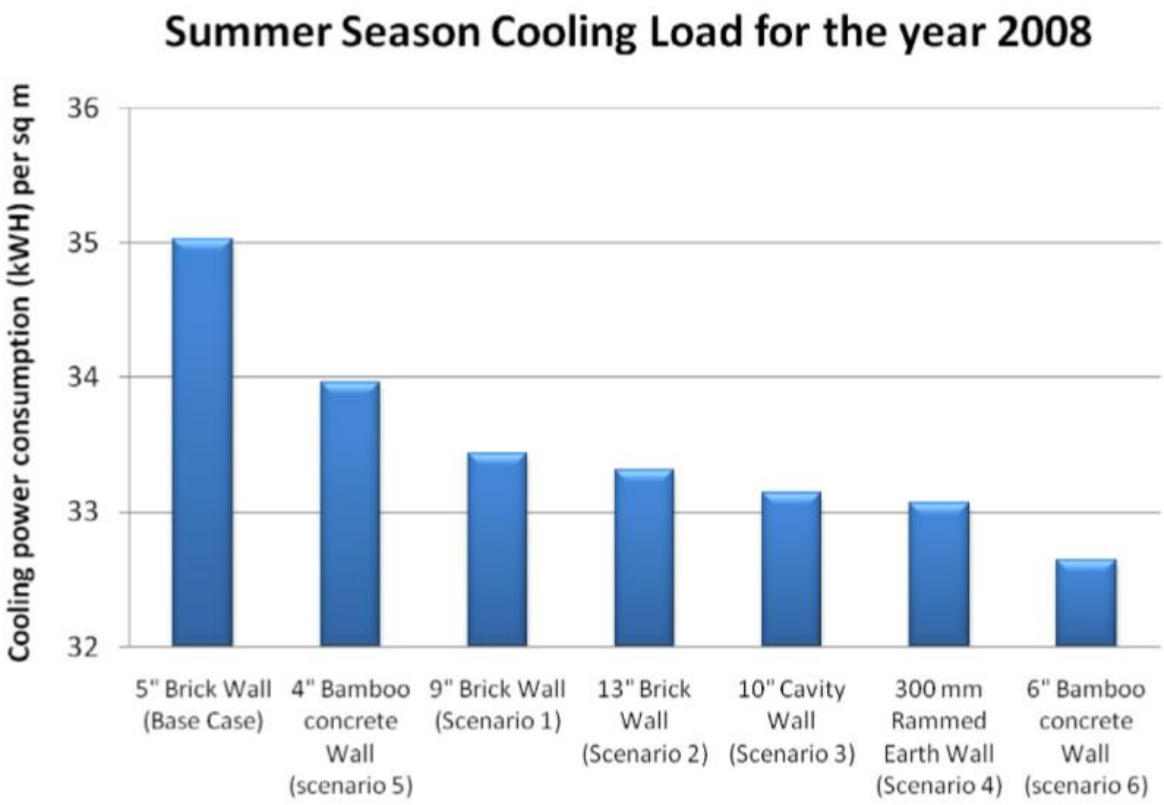

Figure 2 - Simulated cooling load for summer 2018 (Kandya & Mohan, 2018)

Newer materials such as bamboo-concrete composite known as “bamcrete” can help reduce cooling energy consumption and mitigate UHI. The 6-inch-thick wall (scenario 6) as stated previously has a reduction of 7.5% compared to the typical 5-inch brick wall. However, while doubling the thickness of a plain brick wall does reduce energy consumption, further increasing thickness does not have a significant decrease in consumption. However, introducing a wall cavity (scenario 3) yields the highest benefits improvement in thermal resistance using solely brick and plaster. While rammed earth (scenario 4) is also a promising material and is of median cost (Figure 3), its large footprint requirement is not attractive in an urban environment

where minimizing space usage is necessary (Kandya & Mohan, 2018).

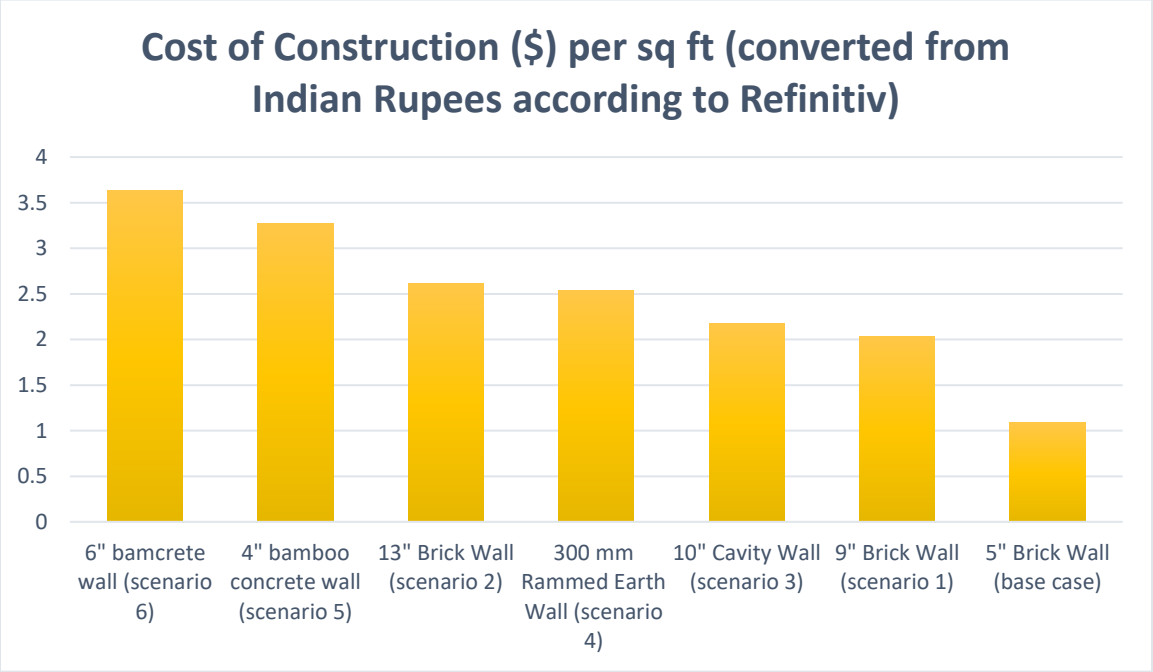

Figure 3 - Cost of construction (Kandya & Mohan, 2018)

These new materials and test results present possibilities to find viable solutions to mitigate the UHI problem in urban areas.

1.1.5 Discussion of Urban Heat Island Effect contributions from existing buildings

A study by Magli et al. (2015) quantified how much heat buildings could contribute to UHI. They also looked at how much a typical building loses heat and applied several heat mitigation techniques to the computer simulation for comparison. The researchers note that despite the complexity of UHI, there is a correlation between anthropogenic heat released by buildings and the formation of UHI. To determine the heat loss, the building envelope and heating, ventilation, and air conditioning (HVAC) were accounted for while the longwave radiation was not considered since it was irrelevant to the UHI effect as per the author. For many

years, researchers collected hourly weather data including global radiation, dry bulb temperature, wind speed, and relative humidity, and incorporated all into a simulation of the chosen building's heat loss by the TRNSYS 17 dynamic thermal modeling software. The main building envelope components thermal transmittance values,'*U*', are: for concrete and light insulated external walls (Uw = 0.52W/(m^2 K)), a non-insulated roof (Ur = 1.32W/(m^2 K)), with north-oriented windows, and double glazed windows (Ug = 2.83W/(m^2 K), g = 0.45). The external concrete walls layer is gray, while the roof waterproof coating is dark. The different cases for heat loss analyzed for this study are:

- The current building (Case B)
- Building with a cool roof (Case CB)
- Building with insulation (Case IB)
- Building with a cool roof and insulation (Case CIB)

The study presented several findings. As shown in Figure 4, utilizing cool roof construction and insulation lost the least amount of heat by both envelope and air-conditioning (AC) systems out of the three modifications for the summer.

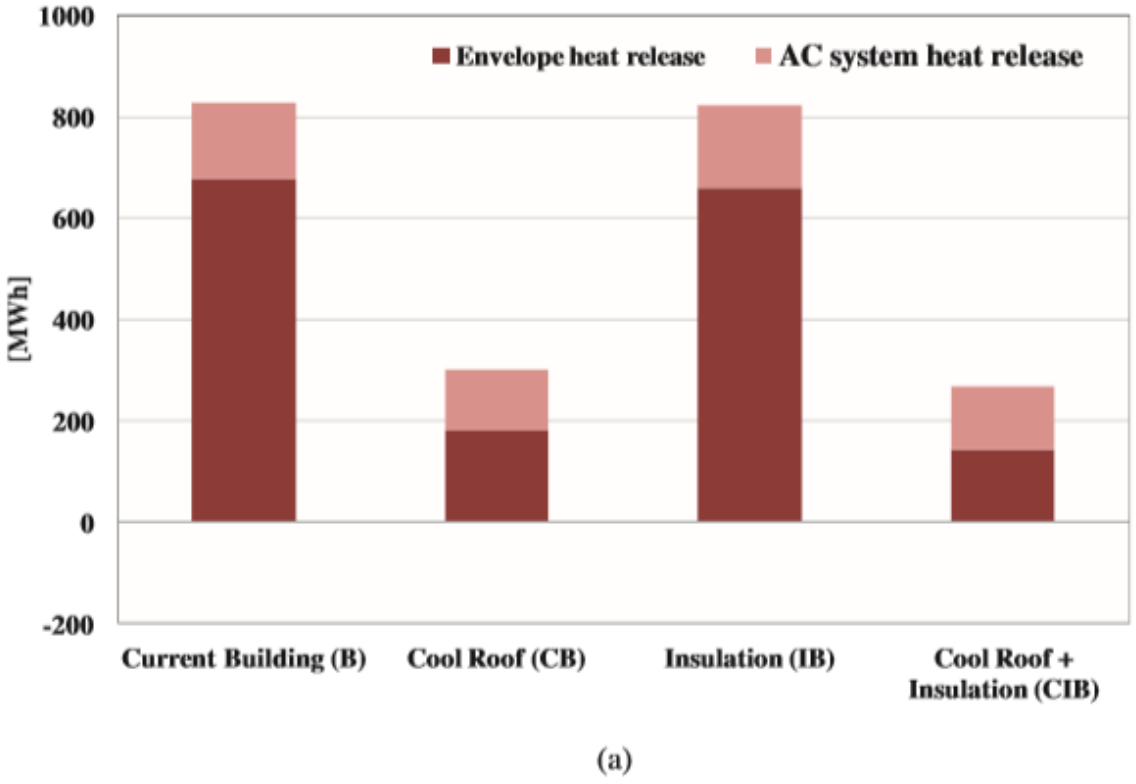

Figure 4 - Total heat released to the environment in the summer (a) periods (Magli et al., 2015)

The simulation results show that in the summer heat released by the building surface is noticeably higher than heat released by AC units. The data also show that improving the insulation of the building alone (case IB) has a lower benefit for UHI management compared to the application of the cool coating to the roof. The cases CB and CIB which involved coatings had an average heat loss reduction of about 63% by the envelope and 20% by the AC system compared to the current building.

The winter heat loss data (Figure 5) showed an interesting trend. The heat loss of the building envelope and the heating system was lower than those of summer but the two cases using cool roof coatings (CB and CIB) showed a negative heat flux (Figure 5). This is beneficial as it could reduce the outside temperature as well as the localized UHI surrounding the building.

The highly insulated case which included the Cool Roof coating and building envelope insulation saw the best results of the four cases.

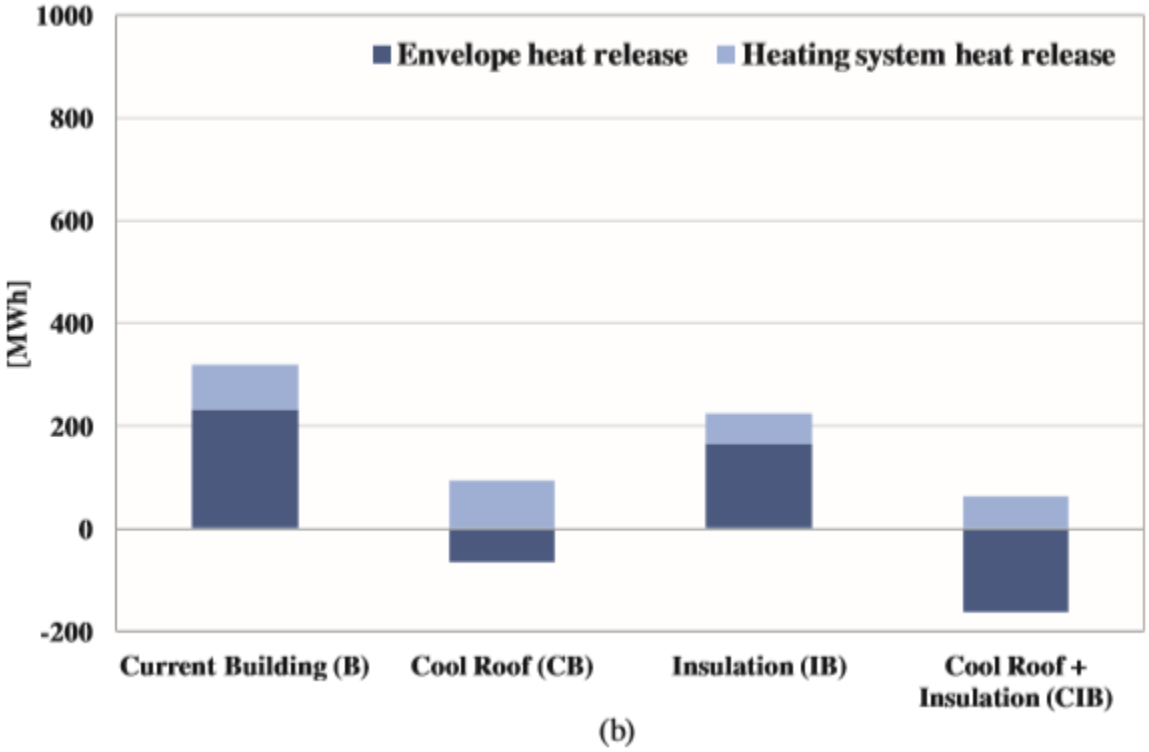

Figure 5 - Total heat released to the environment in the winter periods (Magli et al., 2015)

Figure 6 shows the roof surface temperature simulated for three normal summer days in August 2016. It also suggests that adding insulation alone does not significantly decrease the temperature of the roof compared to the base case since the average and peak daily decrease were only .4°C and 1.3°C, respectively. In contrast, the daily roof surface temperature of the cool roof cases (CB and CIB) showed a reduction of the average and peak daily temperatures by 10.4°C and 20.5°C, respectively. This suggests that the best results include both improving the

insulation of the building as well as improving the reflectivity of the roof.

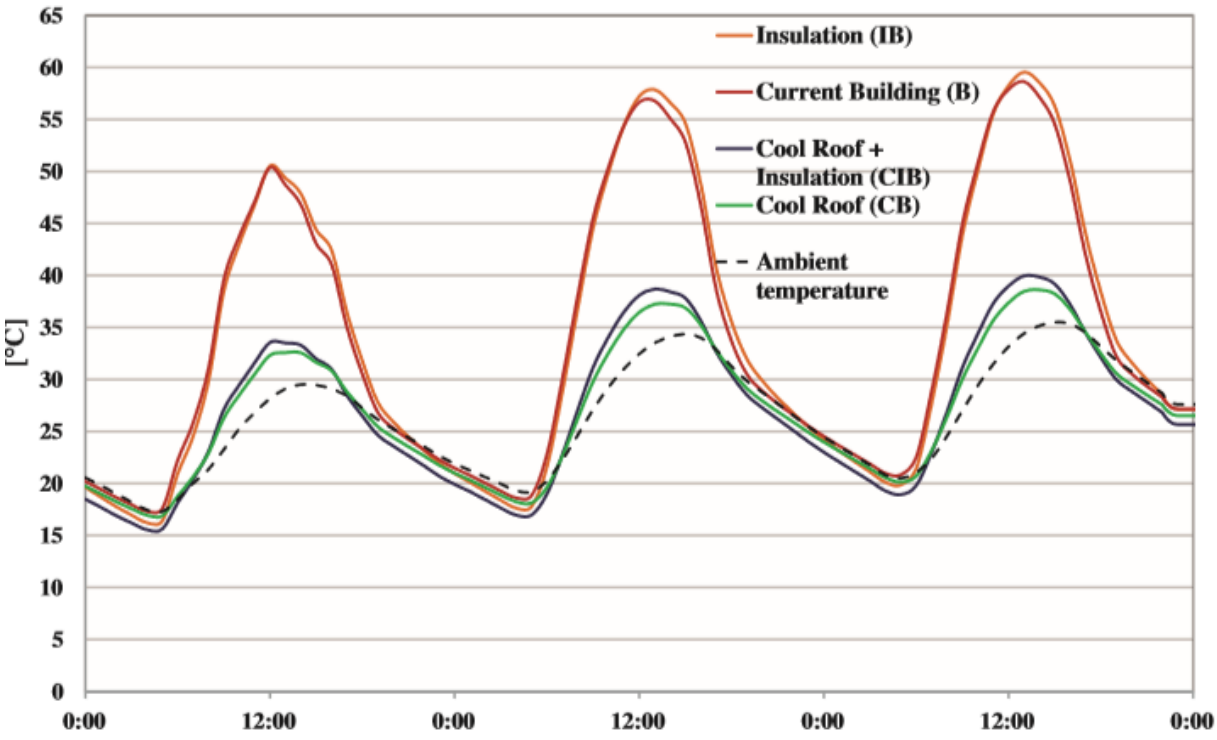

Figure 6 - Average ambient and external roof temperature profiles simulation for three summer days (Magli et al., 2015)

To further emphasize the importance of envelope heat release, Figure 7 shows a comparison between the 15-day moving average trend of the heat released by the building envelope and the HVAC system. Also, the authors noted that increased use of cooling materials in the HVAC systems does not necessarily increase heat loss during wintertime.

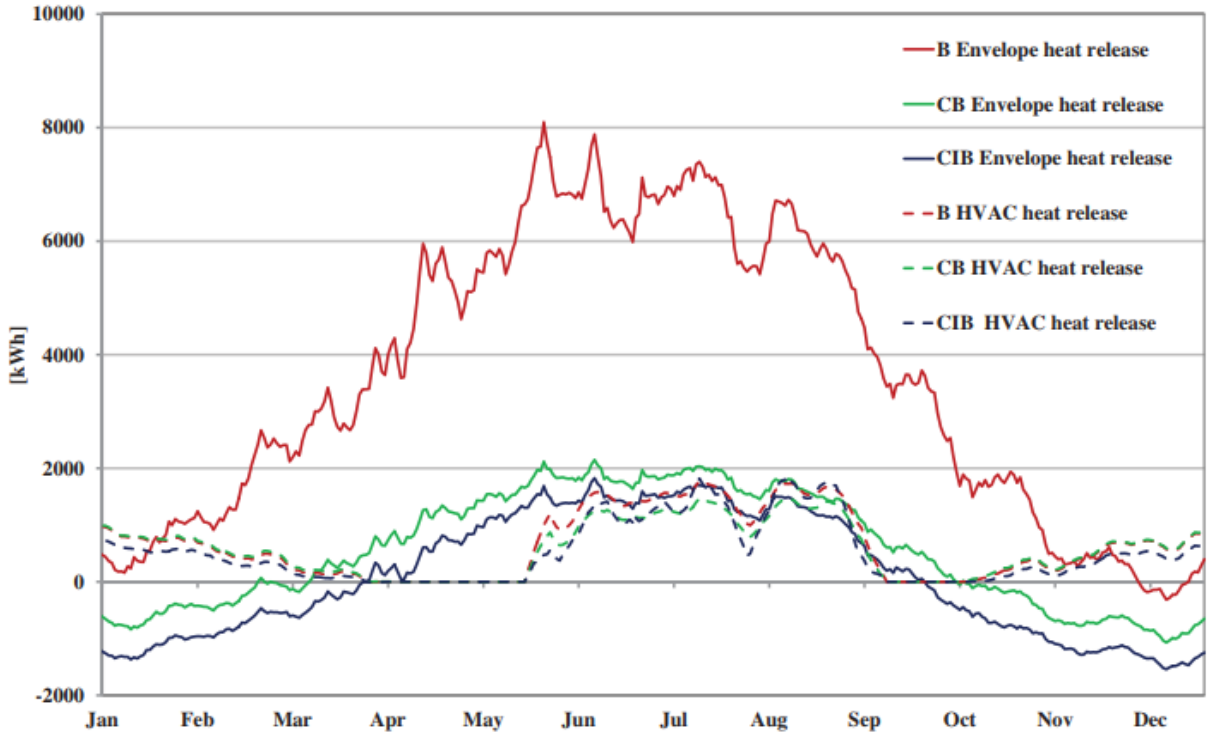

Figure 7 - Heat released by the building envelope and HVAC system for all cases with 15-day moving average trendlines (Magli et al., 2015)

This research suggests that decreasing the overall thermal conductivity of the building envelope combined with roof coatings to increase reflectivity can decrease anthropogenic heat released by the building and the HVAC system. This appears to agree with research by Wonorahardjo et al. where their comparison of buildings made with brick versus multiplexes made with sandwiched walls with glass wool suggested that adding one-way thermal insulation to the envelope can allow the envelope wall to gain heat but inhibit reemitting it to the outside (Wonorahardjo, et al., 2019). A separate study by de Morais et al. found that reducing the thermal conductivity of their model ten times (including the walls of buildings, the street, and roofs) saw a reduction in the UHI intensity by up to two degrees Celsius in the metropolitan center of São Paulo (de Morais, et al., 2019). Additionally, combining reduction of thermal conductivity with increasing surface

albedo (a measure of solar reflectivity), emissivity, and thermal capacity could reduce the UHI intensity by up to three degrees Celsius (de Morais, et al., 2019).

1.2 Thermal Properties of Italian Made Bricks

Properties like thermal conductivity are of concern since it can affect the purchase of insulation, as well as the energy consumption needed to maintain a consistent temperature inside the building. Researchers such as Dondi et al. have published an inquiry into properties that affect thermal conductivity to understand how to improve the performance of clay bricks (Dondi et al., 2004). For their research, they sought to analyze various factors to determine the effect they have on the thermal properties of clay bricks. To achieve this, they collected 29 samples of clays from 21 different brickworks to get a wide range of samples in the Italian brick industry. After grinding and polishing the brick samples to the desired geometry (disks of 200±1 mm diameter, 20±2 mm of thickness, 0.05% planarity), they determined the phase composition, open (where fluid flow is possible), closed (where the fluid flow cannot occur), and total porosity, bulk density, pore size distribution, and pore specific surface.

For this study, the measured thermal conductivity of the bricks was determined by the hot plate method (Ente Nazionale Italiano di Unificazione (UNI) 7745, 1997). The samples measured displayed a sizeable variety of thermal, compositional, physical, and microstructural values. To determine a correlation between bulk density and thermal conductivity, the researchers compared their data to other findings in the available literature. The researchers found that the correlation between bulk density and thermal conductivity was weak as shown below with an r-squared value of about 42% (Figure 8). This indicates that the relationship

between the two variables is not statistically significant.

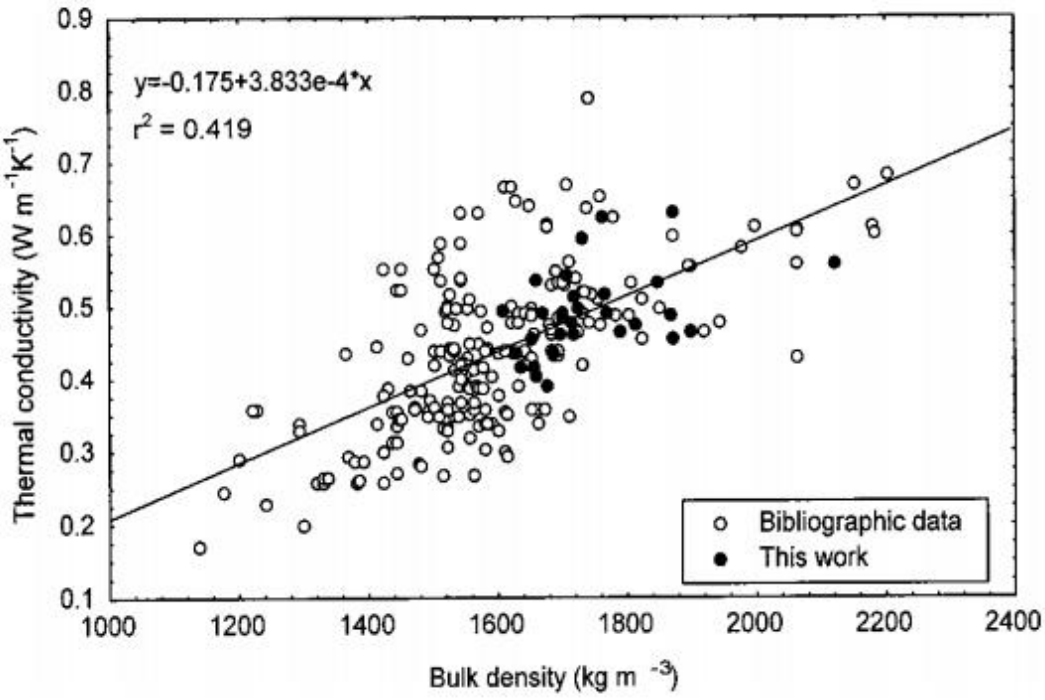

Figure 8 - Thermal conductivity versus bulk density (Dondi,2004)

The weakness of their correlation is further shown as the researchers state that when there was similar bulk density, the bricks' behavior widely varied, implying that more complex variables such as microstructure may be a factor. While this article did not find a sizable relationship, it shows that research is warranted in a possible link between microstructure and thermal conductivity (Dondi et al., 2004).

1.2.2 Discussion of Study on Thermal Conductivity of Thermal Insulation Masonry Bricks

As per the study discussed previously, the thermal property is an important feature of building materials that have been experimented on. A separate study by Pavlík (2013) used a steady-state experiment to determine the effective thermal conductivity of a thermal insulation

masonry brick block with internal cavities manufactured by a Czech company. The width was specified as 500 mm with additional physical properties shown in the table below (Table 2).

Table 2 – Physical properties of brick

Total open porosity (%m^3*m^{-3}	Matrix density (kg*m^{-3})	Bulk density (kg*m^{-3})
1389±14	2830±28	50.9±1.0

The team conducted their experiment by having two commercial climatic chambers, capable of controlling relative humidity and temperature, along with a thermally insulated vapor-proof tunnel to place the samples into. The testing apparatus is shown below (Figure 9).

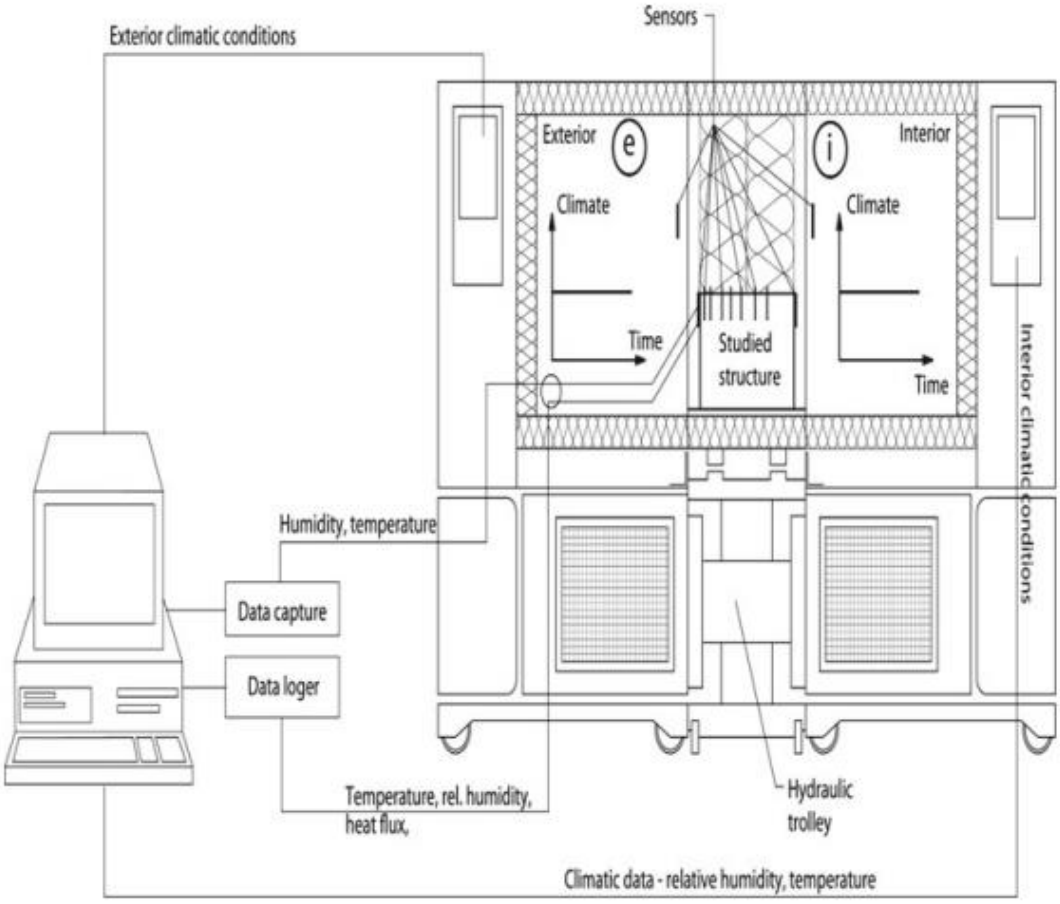

Figure 9- Schematic of the measuring system (Pavlik,2013)

The experiment had both chambers maintain a constant temperature of 30±0.4 °C and 15±0.3 °C, respectively. Additionally, a constant relative humidity of ±1 % was sustained in both chambers to prevent humidity from influencing the heat transfer rate during the 25 days of the experiment.

Equation 3- The thermal conductivity was calculated by Fourier's law

$$q = -\lambda grad(T)$$

After achieving steady-state heat fluxes on both surfaces of the brick, Pavlík and their team determined an effective *k*-value of $.125 \pm .006 \frac{W}{m*K}$ for Heat Flux Sensor 1 (T1) and $.123 \pm .006 \frac{W}{m*K}$ for sensor 2 (T2). This *k*-value is less than the range of *k* according to the Engineering Toolbox. The thermal conductivity study by Pavlik and their team (Pavlík, Fiala, & Černý, 2013) necessitates further research on the effect of cavities on the thermal properties of bricks. Continued research into the field of thermal properties of building materials can be beneficial to brick buildings by providing tools to reduce the amount of needed insulation and energy consumption.

1.2.3 Discussion of Study to Determine Thermal Diffusivity, Specific Heat, and Thermal Conductivity of Bricks of Different Clays

Another study into the measurement of the thermal properties of bricks was done by French and Moroccan researchers (Laaroussi et al., 2014). The researchers conducted measurement of clay brick samples (originating from a Moroccan factory) of two dissimilar sizes using a transient, steady-state hot plate, and flash methods. The goal was to measure the thermal diffusivity ''a'', specific heat ''c'', and thermal conductivity ''k'' of the clay for designing purposes (Laaroussi et al., 2014).

The composition of the clay brick samples is given in Table 3.

Table 3- Percentage of the composition of brick used (Laaroussi et al.,2014)

Type of clays	Red clay	Gray clay	Yellow clay	Clay cellars
Composition of mass	57.14	14.28	14.28	14.28

The dimensions and densities of the samples are displayed in the table below (Table 4).

Table 4- Dimensions and Density of the sample bricks

Samples	Sample 1	Sample 2
Dimensions (mm^3)	100 x 100 x 26	100 x 100 x 21
Density ($kg\ m^{-3}$)	1777	1652

To determine the thermal conductivity of the samples, the researchers used the steady-state, hot plate method (HPS). This consisted of measuring temperature in the center of the heating element between the sample and an insulating polyethylene foam of the same cross-sectional area as depicted in Figure 10. The thermal conductivity of 10 mm thick foam is .04 $W\ m^{-1}\ K^{-1}$.

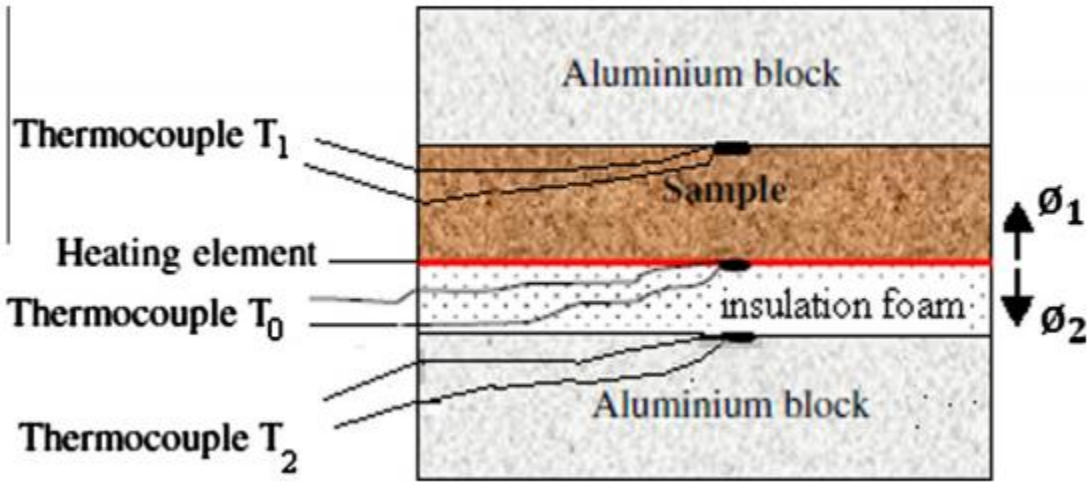

Figure 10 - Graphic depiction of the hot plate method

The hot plate thermal conductivity experiments were done three times to estimate measurement errors and standard deviation as shown in the table below (Table 5). The average thermal conductivity (λ) of the clay was determined by averaging the mean thermal conductivity of the two samples, yielding λ_{HPS} =.35 W m^{-1} K^{-1} and the error is defined by the following Equation 4.

Equation 4 – Error equation

$$(\lambda_{1,2} - \lambda_{HPS})/\lambda_{HPS} = Error$$

Table 5 - Results of Laaroussi et al.

Experiment Number	λ (W m-1 K-1)
Sample 1	λ1
1	0.344
2	0.345
3	0.35
Mean	0.346
Standard Deviation	0.63%
Sample 2	λ2
1	0.358
2	0.352
3	0.349
Mean	0.353
Standard Deviation	1%

The final experimental results of the measurements of thermal conductivity, diffusivity, and heat capacity of the two samples are compared in Table 6. Measurement errors were within 3%, which is better than the global uncertainties at about 7% for transient prediction of thermal properties of clay for brick manufacturing (Laaroussi, Lauriat, Garoum, Cherki, & Jannot, 2014).

Table 6 - Further Results (Laaroussi et al., 2014)

Methods	Sample 1			Sample 2		
	$\lambda\left(\frac{W}{mK}\right)$	a E-7 (m^2/s)	ρc E6 $\frac{J}{m^3K}$	$\lambda\left(\frac{W}{mK}\right)$	a E-7 (m^2/s)	ρc E6 $\frac{J}{m^3K}$
Differential scanning calorimeter (DSC)			1.458 (2.8%)			1.356 (.5%)
FLASH		2.439 (1.1%)			2.591 (3.3%)	
Asymmetrical transient Hot Plate method (HPT)	0.342	2.412	1.418	0.342	2.509	1.363
Steady-State Hot Plate method (HPS)	.346 (1.17%)			.353 (3.2%)		

1.3 Usage of Ready-Made Concrete

The usage of quick setting concrete, also known as ready-made concrete, is widely used for small home improvement projects. However, the material has seen usage in research for its accessibility. For example, researchers Lin Shou et al. 2014, used quikrete in research on the release of ammonia gas from concrete made with ammonium contaminated fly ash (65-3200 mg NH_4^+/kg fly ash) (Shou, et al., 2014).

In another study, researchers used ready-made concrete to examine the effect of replacing sand with porcelain waste in the dry concrete mix. In their experiment, the amount of cement and superplasticizer (SP) the same and only changed how much sand was replaced with porcelain waste. As porcelain waste was increased in samples, the thermal conductivity increased up to 2.41 (W/(m*K)) at 50% replacement of sand with superplasticizer. This increase in thermal conductivity occurred in part due to the chemical reaction of the SP with the concrete mixtures created continuous three-dimensional SP molecules that increased the binder system (Jasim et al., 2019).

An experiment that utilized organic hemp fibers in ready-made concrete (hempcrete) examined the effect of compaction on its mechanical and thermal properties. The authors note

that this hempcrete has a smaller ecological impact as it reduces overall Portland cement used in the concrete. Due to the low density and high porosity of the added hemp fibers, less dense concrete is made which decreases the thermal conductivity ranging from 0.06 to 0.19 (W/(m*K)) (Nguyen, et al., 2010). Consequentially, this also leads to a degradation of strength compared to typical building materials like unaltered concrete (Elfordy et al., 2008).

Another instance of quikrete use in research was presented by Becknell et al. (2006) at a presentation for the American Society for Engineering Education where civil engineering students experimented in creating their own "Greencrete" by modifying the composition of cement mix by replacing some of the mix with other materials such as fly ash, coarse/fine aggregate, and slag cement (Becknell, et al., 2006). Following curing for 14 days, the compressive strength of their greencrete mixtures was measured and compared. The authors conclude that current and future engineers must also consider the environmental impact of materials they choose in their designs. By introducing students to the idea of "green" materials in addition to the economic sphere of material design through their group project, these future engineers will choose less damaging materials and consider the economic cost and benefits of their choices (Becknell, et al., 2006).

Concerning whether quick-set concrete is comparable to standard concrete, researchers Landwermeyer and Rice compared quick-set and regular controlled low-strength materials (CLSM), a runny concrete mix, for municipal repair projects. The study involved determining the bearing strength with the California bearing ratio and subgrade modulus in addition to the penetration resistance and unconfined compressive strength. One of the key results was the early penetration resistance with the quick-set CLSM achieving 400 pounds per square inch in 1/3 to six hours compared to regular CLSM obtaining the same results in fourteen days. The

researchers ultimately concluded that the quick-set concrete mixes were suitable to use for community infrastructure repairs based on standards of ease in future excavation and early minimum specified strength (Landwermeyer & Rice, 1997). In another study, researchers

Gandage et al. analyzed self-compacting concrete and determined a thermal conductivity value of 3.115 $\frac{W}{mK}$ for an M-40 100% Cement Self Compacting Concrete using the guarded hot plate method (Gandage, et al., 2013).

1.4 Discussion of Properties of Palm fiber

According to a study analyzing the effect of layering patterns on properties of epoxy reinforced palm fiber, the density of palm fiber ranges from .7-1.55 g/cm^3 (Jawaid & Khalil , 2011). This is relatively low compared to the density of aluminum is 2.70 g/cm^3 and makes the material look promising to modify concrete samples with (Callister & Rethwisch , 2007). Additionally, the low thermal conductivity of palm fiber at .024 W/mK lends more evidence that utilizing palm fiber may produce attractive results when the modified concrete results are tested (Raut & Gomez, 2016). Another appealing trait of palm fiber discussed in a study on its chemical composition found that the average tensile strength of the fiber tested was 221 MPa with an average elongation at break percentage of 18.9%, compared to cotton fiber which has a tensile strength of 287-597 MPa but an elongation at break percentage of 3-10% (Huzaifah M. R. et al., 2017). These properties, along with their resistance to thermal degradation with an average weight loss percentage from 30-110 °C of 12.69% make palm fiber look like a viable candidate to modify concrete with (Huzaifah M. R. et al., 2017).

This research study summarized in this thesis aimed to build off existing investigations which postulated that there are benefits to adding organic matter to building materials (Kandya & Mohan, 2018) Previous research analyzed the effect of compaction on concrete mixed with hemp

fibers in the interest of creating less environmentally taxing materials (Nguyen, et al., 2010). Other research focused on how improvements in the thermal conductivity of materials could affect energy usage using computer models (Magli, Lodi, Contini, Muscio, & Tartarini, 2015). This thesis, however, presents a comparison of how adding palm fiber affected the thermal conductivity of quick-set concrete.

The organization of the remainder of this thesis is as follows: Chapter 2 explains the sample production process, as well as the testing setup and the experimental procedures. Additionally, Chapter 2 discusses how the final results were calculated from the experimental data. Chapter 3 describes the process of how the calculated data were analyzed using statistics. A discussion of the results and statistical analysis from testing is presented in Chapter 4. Finally, Chapter 5 summarizes the conclusions from this work's study.

CHAPTER II

EXPERIMENTAL METHODOLOGY

2.1 Prepping of Palm Fibers

To obtain evidence that adding palm fiber reduces the thermal conductivity of quick-set concrete samples, the following experimental and analytical methods were followed. For this research, mature Queens Palm fronds that were still green were harvested. Previously published research showed that the most mature leaves that are still attached to the tree have the best mechanical properties and thermal degradation resistance compared to dead or younger leaves (Ishak, Sapuan , Leman, Rahman, & Anwar, 2012). The oldest leaves can be identified as the ones lowest on the trunk, as the younger ones grow from the top and migrate "downwards" as the tree continues to grow. After harvesting the oldest leaves from the leaf base, they were air-dried for 24 hours, based on earlier research that analyzed various properties of a different palm species, before cut into smaller pieces to fit in a multibladed blender (model 50200, Hamilton Beach, Mexico) to an approximate length of 10.75 mm and thickness of .87mm (Huzaifah, Sapuan, Leman, & Ishak, 2017).

2.2 Sample Molds

The molds for the samples were made from polyvinyl chloride (PVC) piping with a diameter of one inch and schedule 40 thickness, cut to a length of 45 mm. To briefly explain, a pipe’s

schedule is a dimensionless number that is the product of dividing the pipe's service pressure by the allowable stress, both in pounds per square inch, which is multiplied by one thousand (Deepak Steel (India), 2020). This length is longer than needed as the final samples were later cut to an approximate height of 32 mm after the concrete cures in the PVC molds. PVC was chosen as the molding and insulating material as it has a lower thermal conductivity value (k) than concrete (Engineering ToolBox, 2003).

2.3 Making of Quick-Set Concrete Sample

a) The nine in total concrete samples were made using a quick-set concrete mix (No 1004, Quikrete, Georgia) and palm fibers (PF). Quick-set concrete was chosen due to the accessibility of the material as well as its workability. The three control samples, with no added PF, were made using 6.25 lbs. of concrete mix per one and a third cup of water and was mixed until well combined. This mix to water ratio was used as the ratio given by the instructions of the quick-set concrete purchased (6.25 lbs. per one cup of water) had difficult workability and samples produced were more brittle compared to the final samples. Following mixing, the PVC molds were filled with the wet concrete mix and packed by pounding the mold on the table several times to ensure uniformity and minimal air pockets.

b) The first three PF modified samples were derived by replacing 0.1% weight of the total concrete mix with PF. This value was chosen through trial and error as an earlier experimental value of 1.0% weight of PF overwhelmed the wet concrete mix and absorbed the water to where the experimental samples could not be molded into a proper

shape. In the case of the control trial where 6.25 lbs. of dry concrete was made at a time, .00625 lbs. of concrete was replaced with PF.

Equation 5 – Weight of palm fibers in .1% PF samples

$$\frac{.1}{100} * 6.25\ lbs. = .00625\ lbs.$$

c) The second set of three PF modified samples replaced 0.5% weight of the dry concrete weight with PF. This value was chosen as it was half of the rejected experimental value of 1.0% and samples made from this value produced workable samples. Similarly, for a 6.25 lbs. dry weight of concrete mix, .03125 lbs. were replaced with palm fiber.

Equation 6 – Weight of palm fiber in 0.5% PF samples

$$\frac{.5}{100} * 6.25\ lbs. = .03125\ lbs$$

.

For each formerly mentioned sample types, they were left to dry for a full 24 hours on a wooden pallet before being removed as detailed in the instructions with the quick-set concrete. The dried intact samples were cut down with a diamond blade saw to create a flat face on both sides of the cylinder samples for a final approximate length of 32.33 mm (± 2.78 mm).

2.4 Laboratory Test Setup

The thermal conductivity of the samples was calculated from measurements gathered with a PA Hilton (Hampshire, UK) Heat Transfer Service Unit (H112) with a Linear Heat Conduction Module (H112A). The H112 unit has been used in similar thermal studies such as researcher Tannouche utilizing the H112 to optimize the roasting of argan kernels (Tannouche, et al., 2015). Additionally, researchers Benham and Rehman used both the H112 unit and H112A attachment to analyze the specific thermal behaviors of 3D printed objects (Benham & Rehman,

2016). The H112 consists of a voltmeter, amp meter, and a temperature reader in Celsius shown in Figure 11.

Figure 11 – H112 Unit from PA Hilton

These have accuracy in readings of .5%, .5%, and ±1.5 °C, respectively (PA Hilton, 2019). The H112A consists of an insulated 25 mm diameter brass heated section and a similarly-sized cooling section which can be clamped with an intermediate insulated section or test specimen between the interfaces. The heated section is supplied by a nominal 75W heater and the cooled section is chilled with water (PA Hilton, 2019). A visual representation of the H112A setup is shown in Figure 12. The two brass sections have three thermocouples spaced 15mm from each other that are connected directly to the H112. There are no thermocouple measurements inside of the samples as it would compromise the PVC used as thermal insulation

for the samples. The process of measuring data to calculate the thermal conductivity value consists of the following steps (PA Hilton, 2019).

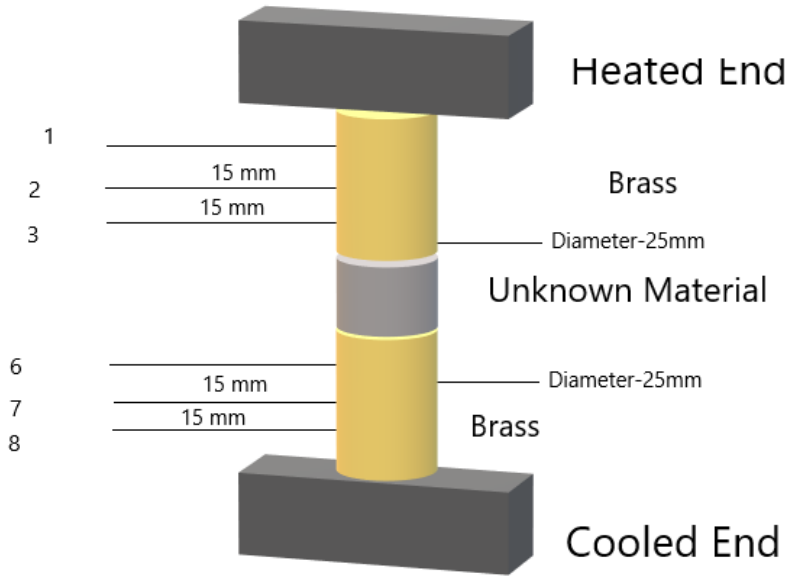

Figure 12 – Schematic of the testing apparatus with numbered thermocouple locations

2.4.1 Measurement Procedures Thermal Conductivity

Before experimenting on the samples, the diameter and height of the samples were measured to ensure proper dimensions of 1 (± 5%) inches diameter and 32.33 (± 2.78) mm height, and their values were recorded. Additionally, the samples were weighed, and their masses were recorded as their dry weight, W_D. The next step was to spread zinc oxide paste on both faces of the sample tested to ensure optimal thermal energy transfer throughout the sample. After spreading the paste, the tested sample was placed with both faces aligned to the H112A and the clamps were used to hold the sample in place during the experimentation process. The water flow to the cooled end of the H112A was turned on and then the H112 unit was switched on. The dial controlling the voltage output was turned until the voltmeter read the first test voltage value of 50V. The machined was left running for 45 minutes while ensuring the voltage remained at 50V. After the set time, the temperature reading of the H112 unit was checked to ensure stability,

and the measurements for thermocouples 1, 2, 3 and 6, 7, 8 (T_1, T_2, T_3, etc.) were determined and by pressing the up-and-down arrows on the temperature-reader of the H112 unit and recorded. Additionally, the current displayed on the amp meter was recorded. The machine and water were turned off for 5 minutes as the H112 unit may overheat and give false readings in later measurements. The earlier steps were repeated at 85V and the thermocouple values and the current were recorded. After the machine was turned off again for 5 minutes, the H112 unit with the cooling water was turned on at 115V for 30 minutes as the voltmeter tends to sputter at that voltage when it runs longer than 40 minutes. The previously noted results were recorded and the H112 unit and the cooling water were turned off.

2.4.2 Compression Strength Measurement Procedure

Compression tests were also conducted using an MTS machine with the assistance of a lab technician from the Mechanical Engineering Department.

2.4.3 Porosity Measurement Procedure

To collect measurements to calculate the permeable porosity of the samples, the standard ASTM-C642 procedure was followed for the cold-water saturation method (CWS) (ASTM, 2006). The samples were submerged in water kept at 19°C for 48 hours. Following the 48 hours, the samples were pat dry with a towel and were weighed. This weight is classified as the saturated surface-dry mass, W_S. Then, using a wire the samples were suspended in water to measure their apparent weight. This is the buoyant mass of the saturated samples, W_B.

2.5 Calculation Methodology

The formula used to calculate the thermal conductivity value of the intermediate sample (k_{int}) was Fourier's law. To briefly explain, Fourier's law of heat conduction states that heat flux

through a material is proportional to the negative vector gradient of temperature (Aboudi, Arnold, & Bednarcyk, 2013).

Equation 7 – Fourier's Law on the intermediate sample

$$\dot{Q} = k_{int} * A_{int}\left(\frac{\Delta T_{int}}{\Delta x_{int}}\right)$$

Where $\dot{Q}$ is the heat flux, *k* is thermal conductivity, *A* is the cross-sectional area of the sample, ΔT is the temperature difference, and Δx is the change in distance.

As shown in Equation 8 below, the heat flux is equal to the product of the current and voltage.

Equation 8 – Power Equation

$$Q = I * V\ (watts)$$

'*A*' represents the cross-sectional area of the sample experimented on with the H112A, in this case, cylinders with a circular cross-sectional area as shown in Equation 9.

Equation 9 – Area of Circle

$$A = \frac{\pi * D^2}{4}$$

'x_{int}' stands for the intermediate distance between the two brass faces in contact with the sample and was calculated using Equation 10.

Equation 10 – Intermediate Distance

$$x_{int} = height\ (h) mm$$

'ΔT_{int}' signifies the temperature difference between the temperatures of the hot and cold brass faces of the H112A unit in contact with the samples. Where the temperatures of those two faces were calculated using Equation 12.

Equation 11 – Intermediate Temperature Difference

$$\Delta T_{int} = T_{hot\ face} - T_{cold\ face}$$

Equation 12 – Hot Face and Cold Face Temperatures of the brass cylinders in contact with the sample

$$T_{hot\ face} = T_3 - \frac{T_2 - T_3}{2}, \qquad T_{cold\ face} = T_6 + \frac{T_6 - T_7}{2}$$

Equation 7 was then rearranged to solve for k_{int} in Equation 13 below.

Equation 13 – Rearranged Fourier's Law equation solving for k_{int}

$$k_{int} = \frac{Q * \Delta x_{int}}{A_{int} * \Delta T_{int}}.$$

Using Equation 12, the temperatures for the hot and cold faces of the brass in contact with the sample were calculated then plugged into Equation 11 to determine the intermediate temperature difference. After using Equation 10 to determine x-intermediate, Microsoft Excel was used to calculate the k-values for each experimental voltage using Equation 13. After determining the k-value of the sample at each test voltage using Equation 13, the values are averaged to determine a k_{int} value for the sample. This calculation method was then repeated for the rest of the samples which yielded three k_{int} values for each category of control, 0.1%, and 0.5%. This process was used to determine the k-values of the samples mixed with PF and compared against the determined k-values of the plain concrete made samples. These values were compared to quantify the effect of mixing PF into concrete based models. If the PF mixed samples had lower k-values, it would indicate that they resist temperature change more than the control samples. In addition, it would lend evidence to suggest the hypothesis that PF mixed in concrete produces samples with lower k-values than plain ones. To calculate the permeable porosity, the weights W_D, W_S, *and* W_B were used in Equation 14 below (Safiuddin & Hearn, 2005).

Equation 14 – Permeable porosity equation

$$Permeable\ porosity(\%) = \frac{W_S - W_D}{W_S - W_B} * 100$$

To calculate the compression strength, the crushing load was divided by the cross-sectional area of the sample tested.

CHAPTER III

STATISTICAL ANALYSIS METHODOLOGY

To determine the significance of the calculated results showing that adding PF reduced the thermal conductivity of quick-set concrete samples, statistical analysis methods were applied. To begin, the standard deviation was calculated by using Microsoft Excel's "STDEV.S" which calculates the sample standard deviation of a given range of values (Microsoft, 2020). Standard deviation quantifies the amount of variation or dispersion in a dataset where a low value indicates that the data tend to cluster around the mean value (Bland & Altman, 1996).

3.1 F-tests

In addition, two *F-tests* were performed comparing the control data with the 0.1% PF data and control with the 0.5% PF data. *F-tests* are used to compare the variances of two data sets with the null hypothesis that they are equal (Ho: $\sigma_1 = \sigma_2$). To briefly explain how the test works, it determines the product of the *mean of squares of the model* divided by the *mean of squares of the residuals* and then compares that ratio to an F-distribution table (Clark, 2018). The tests were executed using Microsoft Excel's "Data Analysis" feature and selecting the "F-Test Two-Samples for Variances" option and selecting the data to be analyzed as shown in Table 19 and 20 of the results. After establishing that the two datasets have unequal variances, a *t-test* was needed to determine if the PF modified samples have a

significant difference from the control samples. T-tests compare the measured mean to another mean such as that of the population or in this case, the control group samples in terms of their standard deviations (Clark, 2018).

3.2 Bonferroni Correction

However, another factor to consider in calculating the t-statistics is how the k_{int} values were calculated. As the k_{int} values are the average of three k-values determined at different test voltages, what's known as "multiplicity" or the "multiple testing problem" occurs when performing multiple subgroup hypothesis testing from the same sample. This can increase the likelihood of incorrectly rejecting a null hypothesis, also known as making a Type I error (Sedgwick, 2012). To compensate for the experimental multiplicity, a Bonferroni correction was made by dividing the alpha level by the number of tests (m) made for each value, in this case, three (Weisstein, n.d.). This adjusted alpha level, $\alpha_{corrected}$, was used to test the level of significance.

Equation 15 – Bonferroni corrected alpha value

$$\alpha_{corrected} = \frac{\alpha}{m} = \frac{.05}{3} \approx 16.67E-3$$

3.3 T-tests

The t-tests were conducted using Microsoft Excel's Data Analysis feature and selecting the "t-Test: Two-Sample Assuming Unequal Variances" choice. Conducting the t-test on the control and 0.1% samples (t-Test 1) yields the output shown in Table 21.

From the output given by the Excel analysis, the values of importance are the "t-Stat" and the "t-Critical two-tail" values. The null hypothesis can be rejected if one of the conditions of the

inequality shown in Equation 16 is met and if the estimated $\alpha < \alpha_{corrected}$ based on the Bonferroni correction.

.

Equation 16 – Conditions to reject t-Test null hypothesis

$$t_{stat} < -t_{critical} \quad or \quad t_{stat} > t_{critical}$$

CHAPTER IV

EXPERIMENTAL RESULTS

The measured thermocouple temperature and electric current values used to calculate the thermal conductivity were collected for each of the nine total samples in this study. Following the calculation methodology detailed in Section 2.5, the results show the effect of adding PF to quick set concrete by comparing the calculated thermal conductivities of three samples each from the control, 0.1% weight PF, and 0.5% weight PF groups. In Table 7 below, the calculated experimental sample, group average k_{int} values, along with their standard deviations are shown.

Table 7 – Data summary table of calculated k-intermediate-values and standard deviation at 45 minutes

Palm Fiber % weight	**Experimental sample k_{int} values (W/(m*K))**			**Average k_{int} (W/(m*K))**	**Standard Deviation**
0 (3 samples)	11.105	11.355	11.791	11.417	0.347
0.1 (3 samples)	9.965	10.646	10.383	10.332	0.344
0.5 (3 samples)	9.743	9.490	9.868	9.700	0.192

As shown in Table 7, as PF is added to the quick-set concrete mix the k-value of the sample decreases. The standard deviations of the modified samples with PF also suggest that the data does not widely vary from each sample and that random error, defined as variations in data due to uncontrollable factors, did not largely contribute to these particular results (Helmenstine, 2020). By replacing 0.1% of the concrete mix weight with PF, the k-value decreases by 9.503% from the control sample. Replacing 0.5% with PF yields a decrease of 15.04%, which in the state

of Texas could save as much as 369,302,1.011 kWh for the total residential consumption of energy. This value was determined using data from the US Energy Information Administration website on the average consumption of energy by residential customers in the state of Texas. The energy savings for an assumed wall surface of 7.4 m^2 with felt insulation ($.04 \frac{W}{m^2K}$) from the control case to the 0.5% PF case were calculated and the same percentage decrease was assumed for the average energy consumption of the state of Texas (U.S Energy Information Administration, 2019). This process is detailed in equation 17 below.

Equation 17 – Summary of energy-saving calculations where air convection was presumed at .5 W/(m^2K)

$$\dot{Q} = \frac{\Delta T}{R_{total}}$$

$$R_{base} = \frac{1}{7.4\ m^2 * .5 \frac{W}{m^2K}} + \frac{.1524\ m}{.04 \frac{W}{mK} * 7.4\ m^2} + \frac{.1125\ m}{11.4 \frac{W}{mK} * 7.4\ m^2} + \frac{1}{7.4\ m^2 * .5 \frac{W}{m^2K}}$$

$$R_{base} = 1.0567 \frac{K}{W}$$

$$R_{0.5\%\ PF} = \frac{1}{7.4\ m^2 * .5 \frac{W}{m^2K}} + \frac{.1524\ m}{.04 \frac{W}{mK} * 7.4\ m^2} + \frac{.1125\ m}{\frac{W}{mK} * 7.4\ m^2} + \frac{1}{7.4\ m^2 * .5 \frac{W}{m^2K}}$$

$$R_{0.5\%\ PF} = 1.0570 \frac{K}{W}$$

$$\dot{Q}_{base} = \frac{(30 - 20)℃}{1.0567 \frac{K}{W}} = 9.4634\ W$$

$$\dot{Q}_{0.5\%\ PF} = \frac{(30 - 20)℃}{1.0570 \frac{K}{W}} = 9.4607\ W$$

$$Percent\ Difference = \frac{\dot{Q}_{0.5\%\ PF} - \dot{Q}_{base}}{\dot{Q}_{base}} * 100 = -.0285\%$$

$$Average\ Montly\ Consumption = 1{,}140\ kWh$$

$$Average\ Montly\ Consumption\ (decreased\ by\ percent\ difference)\ = 1{,}139.68\ kWh$$

$$Base\ total\ consumption = 1{,}140\ kWh * 11{,}366{,}639\ customers = 129{,}579{,}684{,}60\ kWh$$

$$New\ total\ consumption = 1{,}139.68\ kWh * 11{,}366{,}639\ customers = 129{,}542{,}754{,}39\ kWh$$

$$\Delta Consumption = Base\ consumption - New\ consumption = 3693021.011 kWh$$

In initial calculations, the intermediate distance utilized a formula from the H112A user's manual as shown in Equation 17 below.

Equation 18 – Original intermediate distance equation (PA Hilton, 2019)

$$x_{int} = height\ (h) mm + 15\ mm$$

This equation was changed to the value shown in Chapter 2 as the given intermediate distance in the user's manual for the H112A unit, was the distance between thermocouples T3 and T6. These thermocouples are both 7.5 mm away from the faces of the brass cylinders. However, this intermediate distance value included portions of the brass cylinders of the hot and cold sides while Equation 7 used the temperatures of the brass faces in contact with the sample. This error essentially "added on" more material to be analyzed by the equation. The original values calculated with the incorrect intermediate distance value are shown below.

Table 8 – Thermal conductivity values at 45 minutes using incorrect Δx_{int} values

Palm Fiber % weight	**Average k_{int} (W/(m*K))**
0 (3 samples)	16.238
0.1 (3 samples)	15.347
0.5 (3 samples)	14.469

As further plotting of thermal curves revealed, samples heated for 45 minutes do not achieve thermal stability. Therefore, thermal measurements were repeated for one sample from each grouping at 120 and 180 minutes at 50V, and their thermal conductivities were calculated as an estimate of the true thermal conductivity of the samples. These results are further discussed in Section 4.2.

4.1 Physical Measurements and Related Results

Table 9 summarizes the physical dimensions of the nine samples used in this study including their weight, height, and diameter. Control samples are labeled ‘C’, 0.1% weight PF samples are labeled ‘O’, and .5% weight PF samples are labeled ‘F’.

Table 9 – Summary of physical measurements of samples

	Control			**0.1% PF**			**0.5% PF**		
	1C	**2C**	**3C**	**1O**	**2O**	**3O**	**1F**	**2F**	**3F**
Weight (grams)	51	59	60	47	51	48	49	47	49
Height (mm)	33.20	36.32	37.19	29.53	32.63	30.61	31.18	29.92	30.44
Diameter (mm)	25.92	26.45	26.38	25.86	25.73	25.82	26.31	26.19	26.26
Volume (cm^3)	17.52	19.96	20.32	15.51	16.96	16.02	16.96	16.12	16.49

The samples have varying physical properties in part due to cutting the samples by hand which gave the samples varying heights which affected their corresponding volumes and weight.

After the sample densities were determined, as shown in Table 10, the average and standard deviation were calculated to determine their variation amongst all samples. While the physical measurements of the samples such as the weight and height had problematic variations due to cutting them by hand, (σ=4.92, 2.78 respectively) these systemic errors were not reflected as substantially in the density calculations and can be eliminated in future studies by using a stationary diamond saw instead of a handheld type. The standard deviation found for the density of all the samples was much smaller at .05. When the standard deviation was calculated for each PF percentage grouping, despite the smaller sample size, those values were even smaller (σ_C=0.02, σ_O=0.02, σ_F=0.04) which further implies that random error did not severely impact this calculation.

Table 10 – Sample densities, with average and standard deviation value

	Control			0.1% PF			0.5% PF				
	1C	**2C**	**3C**	**1O**	**2O**	**3O**	**1F**	**2F**	**3F**	**Avg**	**STD**
Density (g/cm^3)	2.91	2.96	2.95	3.03	3.01	3.00	2.89	2.92	2.97	2.96	0.05

As thermal conductivity is expected to decrease with more porosity, conversely as density increases it is expected for thermal conductivity to also rise. This correlation between density and thermal conductivity is shown in Ozcan and Korkmaz's research into the thermal and mechanical properties of Uludag fir and black poplar wood. After determining the thermal conductivity using the guarded hotplate method and the density of their samples, the two data values were plotted as shown in Figure 13 for black poplar with a strong r-squared value of 84.1% (Özcan & Korkmaz, 2018).

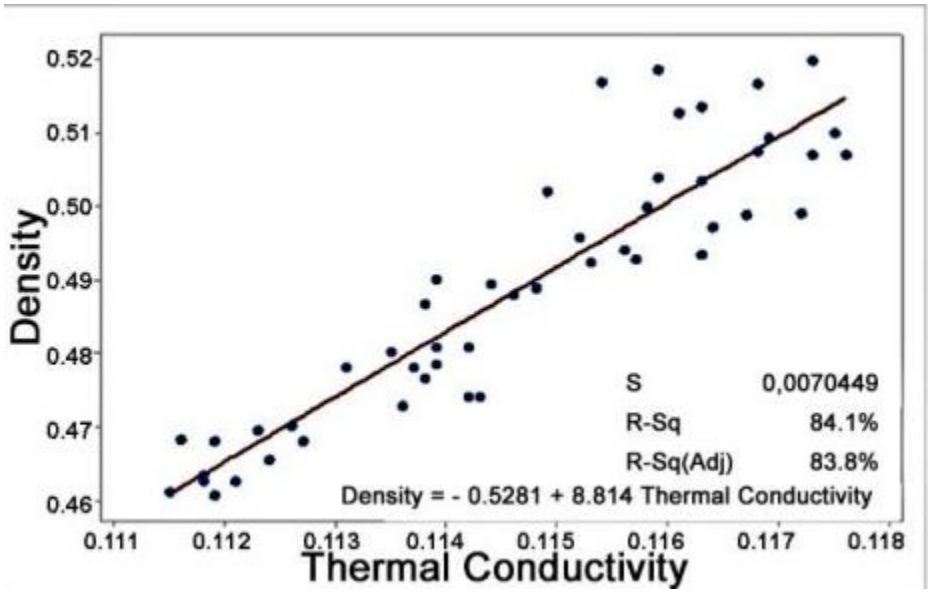

Figure 13 – Plot of thermal conductivity vs density of black poplar wood (Özcan & Korkmaz, 2018)

In this thesis study studying the effect of adding palm fiber to quick set concrete, there was a weak correlation between density and thermal conductivity for all nine samples as shown in Figure 14. Overall, the thermal conductivity does appear to increase as the density of the

samples increases. This is further evidenced by the correlation of the two variables calculated using the "CORREL" function in Excel at 0.0381, suggesting a weak but positive correlation where as density increases the thermal conductivity also rises (Microsoft, 2020). The weaker trend in this study may be due to hand tapping the samples not producing a consistent reduction in air bubbles across all samples in their interiors. Also, dry curing the samples likely lead to the samples losing moisture which leads to inconsistencies within the interiors of the samples of each grouping, affecting their final densities (National Ready Mixed Concrete Association, 2017).

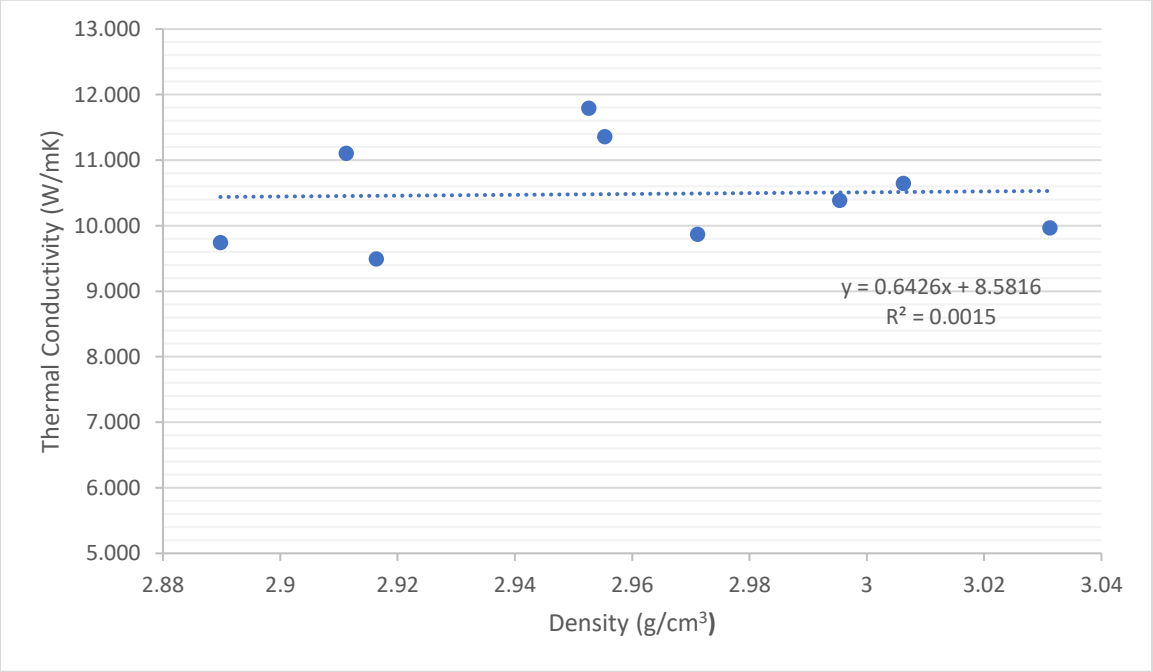

Figure 14 – Graph of the thermal conductivity values of the test samples at 45 minutes vs. density

4.2 Temperature vs. Time Plot

Temperature curves were also measured by running the H112 unit at 50 V with the thermocouple readings recorded at 10-minute intervals for one sample from each grouping in

Figures 15, 16, and 17 along with the data for the 180-minute trials in Tables 11 through 13 below.

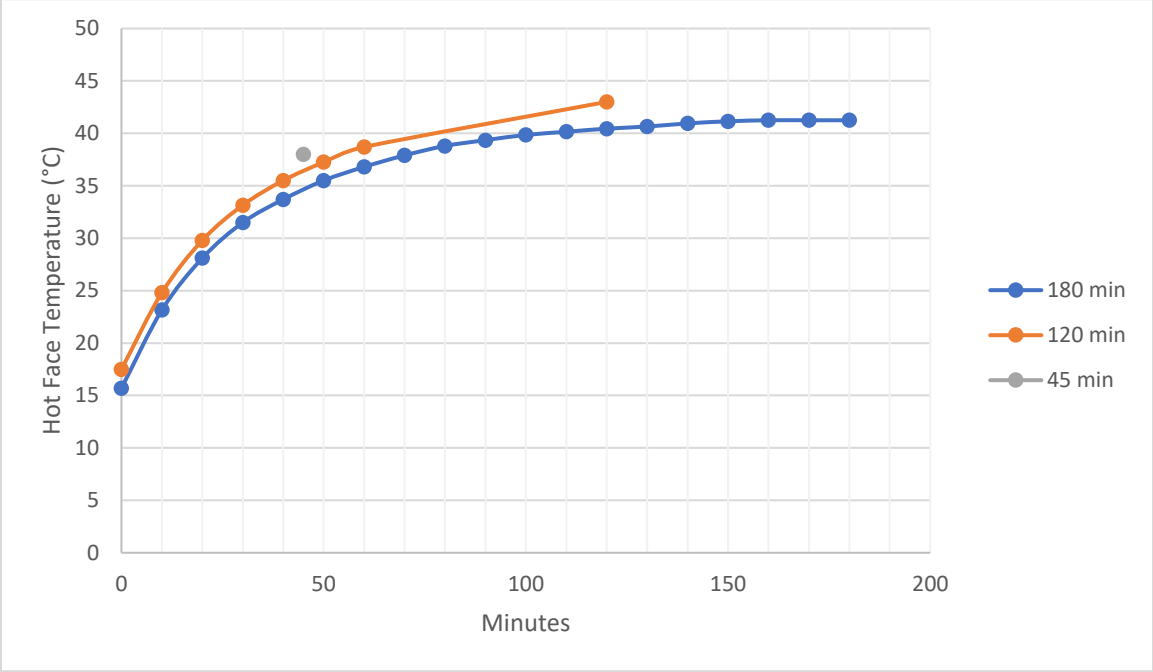

Figure 15 – Graph of the hot face temperature at different test times at 50 V for control sample 1

Table 11 – Temperature data for 180-minute trial in Figure 15

Minutes	T1	T2	T3	T6	T7	T8	T Hot	T Cold	T Hot diff /min
0	15.7	15.7	15.7	15.8	15.8	15.8	15.7	15.8	
10	23.6	23.3	23.2	16.1	16	16	23.15	16.15	0.745
20	28.6	28.4	28.2	16.4	16.3	16.3	28.1	16.45	0.495
30	32.1	31.8	31.6	16.7	16.6	16.6	31.5	16.75	0.34
40	34.3	34	33.8	16.8	16.7	16.7	33.7	16.85	0.22
50	36.2	35.8	35.6	16.9	16.9	16.7	35.5	16.9	0.18
60	37.5	37.1	36.9	16.8	16.8	16.7	36.8	16.8	0.13
70	38.6	38.2	38	16.9	16.8	16.8	37.9	16.95	0.11
80	39.5	39.1	38.9	16.9	16.9	16.8	38.8	16.9	0.09
90	40.2	39.8	39.5	17	16.9	16.9	39.35	17.05	0.055
100	40.7	40.3	40	17	17	16.9	39.85	17	0.05
110	41.1	40.6	40.3	17.1	17	16.9	40.15	17.15	0.03
120	41.3	40.9	40.6	17.1	17	16.9	40.45	17.15	0.03
130	41.5	41.1	40.8	17.1	17	16.9	40.65	17.15	0.02
140	41.9	41.4	41.1	17.1	17	16.9	40.95	17.15	0.03
150	42	41.6	41.3	17.1	17	16.9	41.15	17.15	0.02

160	42.1	41.7	41.4	17.1	17	17	41.25	17.15	0.01
170	42.1	41.7	41.4	17.2	17	17	41.25	17.3	0
180	42.1	41.7	41.4	17.2	17	17	41.25	17.3	0

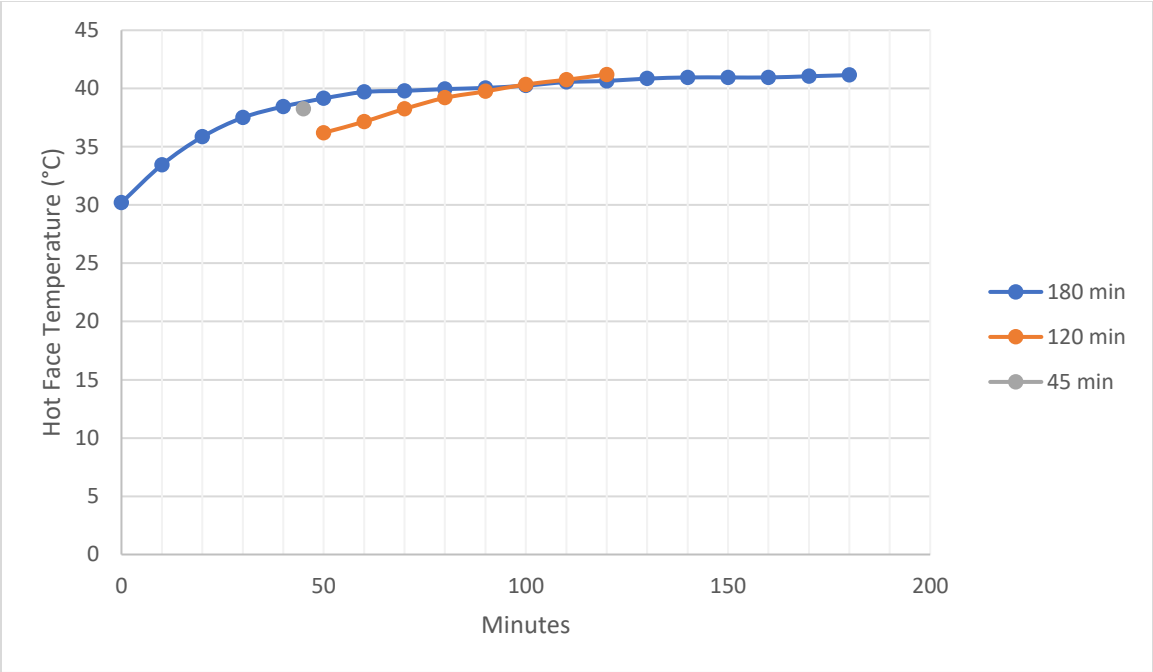

Figure 16 – Graph of the hot face temperature at different test times at 50 V for 0.1% PF sample 1

Table 12 – Temperature data for 180-minute trial in Figure 16

Minutes	T1	T2	T3	T6	T7	T8	T Hot	T Cold	T Hot diff/min
0	31.2	30.8	30.4	16.3	16.3	16.3	30.2	16.3	
10	34.3	33.9	33.6	16.9	16.8	16.7	33.45	16.95	0.325
20	36.7	36.3	36	17.1	16.9	16.9	35.85	17.2	0.24
30	38.2	37.8	37.6	17.2	17.1	17	37.5	17.25	0.165
40	39.3	38.9	38.6	17.3	17.2	17.1	38.45	17.35	0.095
50	40	39.6	39.3	17.3	17.2	17.1	39.15	17.35	0.07
60	40.4	40	39.8	17.3	17.2	17.1	39.7	17.35	0.055
70	40.6	40.1	39.9	17.3	17.2	17.1	39.8	17.35	0.01
80	40.8	40.4	40.1	17.3	17.2	17.1	39.95	17.35	0.015
90	40.9	40.5	40.2	17.3	17.2	17.1	40.05	17.35	0.01
100	41.4	40.7	40.4	17.3	17.2	17.1	40.25	17.35	0.02
110	41.4	41	40.7	17.3	17.2	17.1	40.55	17.35	0.03
120	41.6	41.1	40.8	17.3	17.2	17.1	40.65	17.35	0.01
130	41.7	41.3	41	17.3	17.2	17.1	40.85	17.35	0.02
140	41.8	41.4	41.1	17.3	17.2	17.1	40.95	17.35	0.01

150	41.8	41.4	41.1	17.3	17.2	17.1	40.95	17.35	0
160	41.9	41.4	41.1	17.3	17.2	17.1	40.95	17.35	0
170	41.9	41.5	41.2	17.3	17.2	17.1	41.05	17.35	0.01
180	42.1	41.6	41.3	17.2	17.1	17	41.15	17.25	0.01

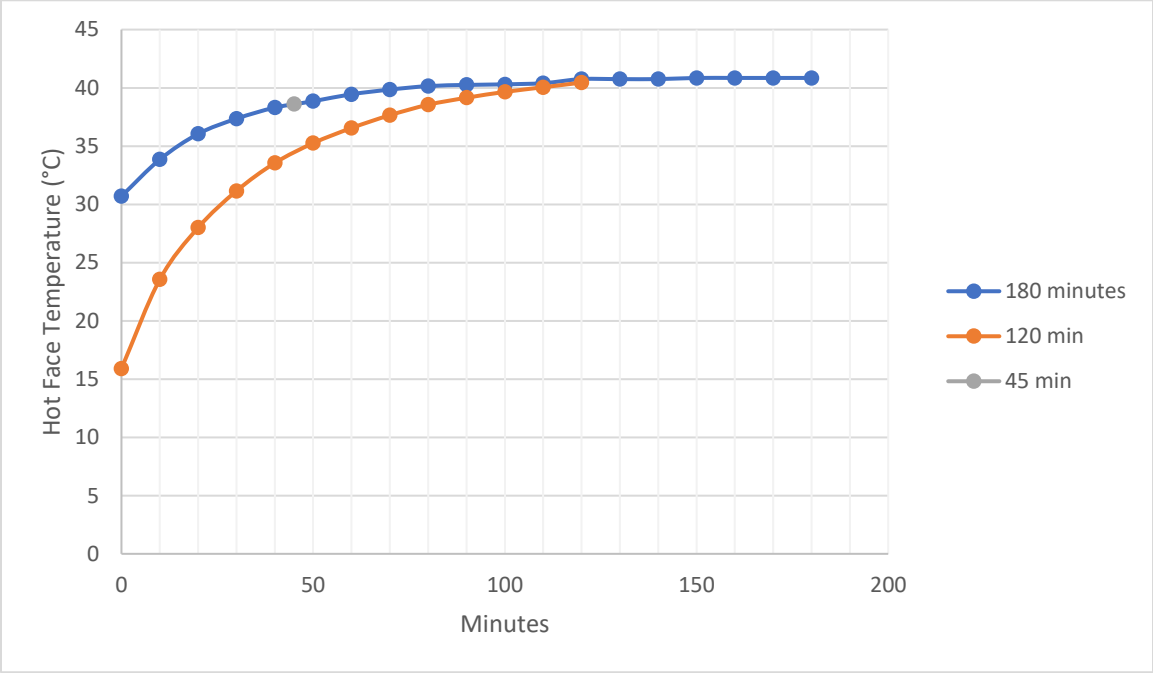

Figure 17 – Graph of the hot face temperature at different test times at 50 V for 0.5% PF sample 1

Table 13 – Temperature data of 180-minute trial in Figure 17

Minutes	T1	T2	T3	T6	T7	T8	T Hot	T Cold	T Hot diff/min
0	31.6	31.3	30.9	16.7	16.7	16.7	30.7	16.7	
10	34.7	34.3	34	16.9	16.8	16.7	33.85	16.95	0.315
20	37	36.5	36.2	17	16.9	16.8	36.05	17.05	0.22
30	38.2	37.8	37.5	17.1	17	16.9	37.35	17.15	0.13
40	39	38.6	38.4	17.2	17.1	17	38.3	17.25	0.095
50	39.7	39.3	39	17.2	17.1	17	38.85	17.25	0.055
60	40.3	39.9	39.6	17.3	17.2	17.1	39.45	17.35	0.06
70	40.7	40.3	40	17.3	17.2	17.1	39.85	17.35	0.04
80	41	40.6	40.3	17.4	17.3	17.1	40.15	17.45	0.03
90	41.2	40.7	40.4	17.4	17.3	17.1	40.25	17.45	0.01
100	41.3	40.9	40.5	17.4	17.3	17.1	40.3	17.45	0.005
110	41.3	41	40.6	17.4	17.3	17.2	40.4	17.45	0.01
120	41.6	41.2	40.9	17.4	17.3	17.2	40.75	17.45	0.035
130	41.6	41.2	40.9	17.5	17.4	17.2	40.75	17.55	0

140	41.6	41.2	40.9	17.5	17.4	17.2	40.75	17.55	0
150	41.7	41.3	41	17.5	17.3	17.2	40.85	17.6	0.01
160	41.8	41.3	41	17.5	17.4	17.2	40.85	17.55	0
170	41.7	41.3	41	17.5	17.4	17.2	40.85	17.55	0
180	41.7	41.3	41	17.5	17.4	17.2	40.85	17.55	0

Following the 50-minute mark, the slope from point to point starts to dramatically decrease with all samples, as shown with 180-minute data. As shown in the earlier thermal plots, a 120-minute trial approaches thermal stability but is assuredly achieved in the 180-minute trials. In the 180-minute trials shown in the preceding tables, thermal stability is achieved around 130 to 160 minutes depending on the sample The temperatures gathered in the 120 and 180-minute trials are used to calculate an estimated thermal conductivity for all three samples in each grouping as shown in Table 14.

While the uncertainty of the previously reported thermal conductivity values taken at 45 minutes indicates they were precise, the systemic error in the methodology of how long the samples were heated resulted in higher thermal conductivity values than the "true values" which are likely closer to the 180-minute trial values shown in Table 14 below.

Table 14 – Summary of thermal conductivities at different trials.

Thermal Conductivity $\left(\frac{W}{mK}\right)$	**Control**	**0.1% PF**	**0.5% PF**
45-minute trial (9 samples)	11.417	10.332	9.700
120-minute trial (1 sample)	7.328	6.996	6.953
180-minute trial (1 sample)	6.961	6.235	6.520

Table 14 compares the thermal conductivities measured at 45 minutes for nine samples to the values found for a single sample at 120 and 180 minutes. While the reported 45-minute thermal conductivity values may be higher than the "true values", which are closer to the 180-minute trial

values, they were calculated using a consistently applied methodology and conclusions can still be drawn that may inform further study. The 180-minute trial samples are still higher than expected from literature, this may be due to the samples being made from a fast-setting form of ready-made concrete that uses no curing procedure and is set in two hours according to the manufacturer (Quikrete, 2020). Typically, industrial concrete and some forms of ready-made concrete use a water-curing process where the concrete is kept moist for up to 28 days which affects the properties of the final material (National Ready Mixed Concrete Association, 2017). According to the National Ready Mixed Concrete Association, cured concrete has more predictable durability and is less prone to cracking than dry-cured concrete, which following was how these samples were cured following the instructions of the manufacturer (National Ready Mixed Concrete Association, 2017). The dry curing of the samples used in this study may have affected the final weight and density of the samples. These effects may have interfered in the measured thermal conductivities of the samples and future studies may determine that wet curing improves the measured thermal conductivity of replicated samples.

4.3 Permeable Porosity

Using the measured weights shown in Table 15 below, the permeable porosity values were calculated using Equation 19 shown again below for reference. The calculated permeable porosity results are shown in Table 16

Equation 19 – Permeable porosity equation

$$Permeable\ porosity(\%) = \frac{W_S - W_D}{W_S - W_B} * 100$$

Table 15 – Measured weights of samples

	Control			0.1% PF			0.5% PF		
	1C	**2C**	**3C**	**1O**	**2O**	**3O**	**1F**	**2F**	**3F**
Dry weight, Wd (g)	51	59	60	47	51	48	49	47	49
Surface dry saturated weight, Ws (g)	53	60	62	48	53	49	51	49	50
Water immersed saturated weight, Wb (g)	28	31	32	26	27	27	27	25	26

Table 16 – Calculated permeable porosity

	Control			0.1% PF			0.5% PF		
	1C	**2C**	**3C**	**1O**	**2O**	**3O**	**1F**	**2F**	**3F**
Permeable Porosity	8.00	3.45	6.67	4.55	7.69	4.55	8.33	8.33	4.17
Standard Deviations	2.34			1.82			2.41		

The calculated porosities are below 10% but with standard deviations for each grouping that vary around two, this suggests that tapping the samples by hand to minimize air bubbles may not achieve consistent results. However, taking the standard deviation of all nine samples yields a standard deviation of 2.00 which may suggest the variation may not be as problematic as suggested when calculated for each grouping. This error could be minimized by increasing the sample size if this were purely random, but this may be a systemic issue by tapping the samples by hand. Future studies should consider using a machine to tap the samples to achieve more consistent porosity results to minimize systemic error from this step. An interesting note is in

research by Safiuddin, using a CWS method to measure the permeable porosity of mixed concrete samples, showed they achieved results above 12% (Safiuddin & Hearn, 2005). Also, they found that reducing the water-cement ratio from .6 to .5 decreased the permeable porosity of samples and their compressive strength was increased.

Comparing the calculated densities and porosities in this study showed a weaker correlation of about 35% as shown in Figure 18. This is likely due to the smaller sample size of nine trials allowing outliers to have a more outsized impact on the regression model.

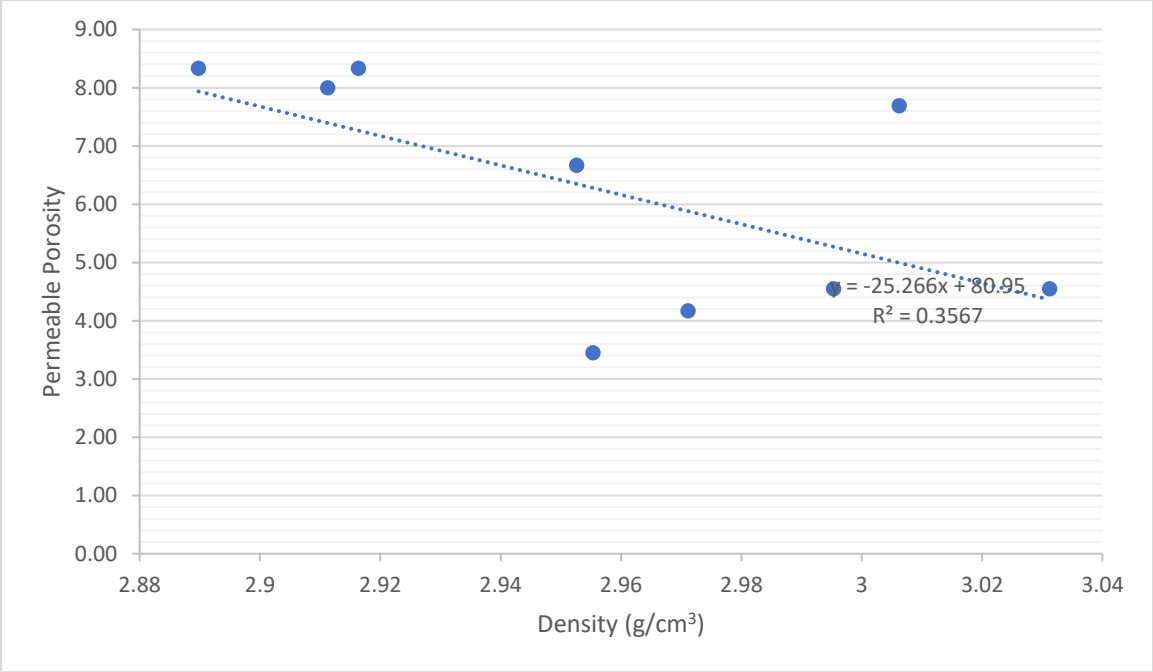

Figure 18 – Graph of the density vs permeable porosity of the nine samples

It is commonly accepted that density and porosity are correlated, where objects with more porosity are less dense. This is evidenced in studies such as by Ghrieb et al. where they analyzed 60 samples to determine the properties of stabilized dune sands mixed with stabilizers, cement, and filtered sand (Ghrieb et al., 2014). Part of their results included a scatterplot and regression model of the relationship between the porosity and bulk density of the tested samples. Their

samples show a strong correlation whereas density increases porosity decreases in Figure 19 (Ghrieb et al., 2014).

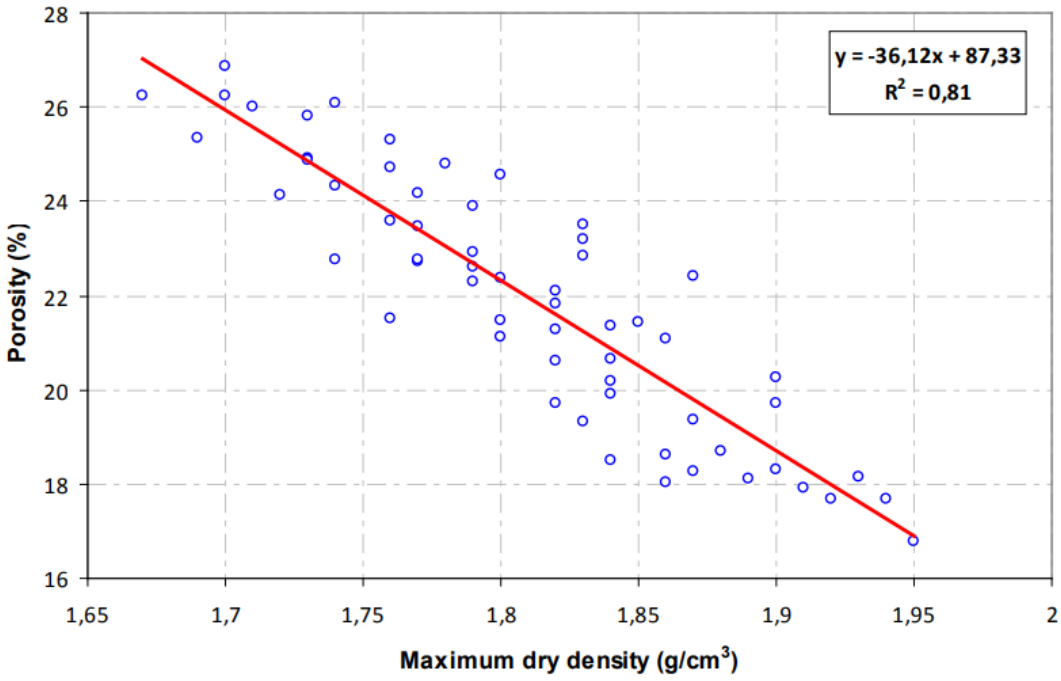

Figure 19 –Graph showing stabilized dune sand sample's dry density vs. porosity (Ghrieb et al., 2014)

Plotting the calculated permeable porosity versus thermal conductivity in Figure 20 yields a graph without a visually discernable trend. Furthermore, calculating the correlation coefficient with the Microsoft Excel function "CORREL" (r= - 0.145), which measures the linear relationship of two variables, suggests that permeable porosity and thermal conductivity are not closely correlated (Microsoft, 2020). Additionally, calculating the determination coefficient (r^2=0.0211), which quantifies how much a linear regression model fits the data, further demonstrates that there is not a strong correlation between the calculated permeable porosity and thermal conductivity values in this study (Devore, 2011). This lack of a trend, however, may more due to the sizable variation in porosity due to the systemic error caused when tapping by hand and does not necessarily reflect the expected relationship between

porosity and thermal conductivity. In addition, dry curing the samples led to cracking across all samples which may have contributed to the inconsistent porosity. These inconsistent porosities when plotted against the thermal conductivities portray a trend that may be uncompliant with wet cured concrete. For example, Demirboga and Kan's research into the thermal properties of polystyrene aggregate concrete, which were wet cured, found an r-squared value between the oven-dry density and thermal conductivity of their samples at .92 (Demirboga & Kan, 2012).

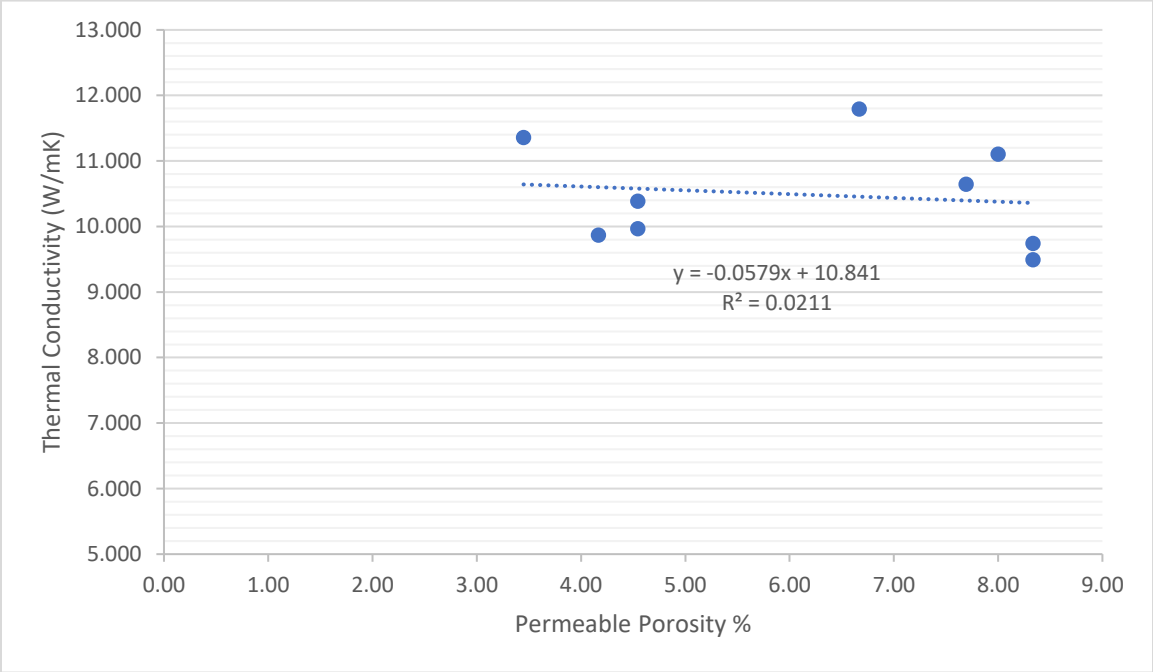

Figure 20 – Scatterplot of permeable porosity (%) vs. thermal conductivity (W/(mK))

Although, the linear regression equation calculated for this model does agree with existing literature that commonly demonstrates a relationship whereas porosity increases, the thermal conductivity decreases. This relationship is demonstrated in Rahmouni et al.'s research on the physical properties of calcarenite rocks. In their research, multiple samples of 7x7x7 cm^3 were extracted from a single block of calcarenite rock and tested to determine their porosity and thermal conductivity values (Rahmouni, et al., 2013). In both dry and saturated samples, there

was a strong correlation between the porosity and thermal conductivity of the samples as shown in Figures 21 and 22 below (Rahmouni, et al., 2013).

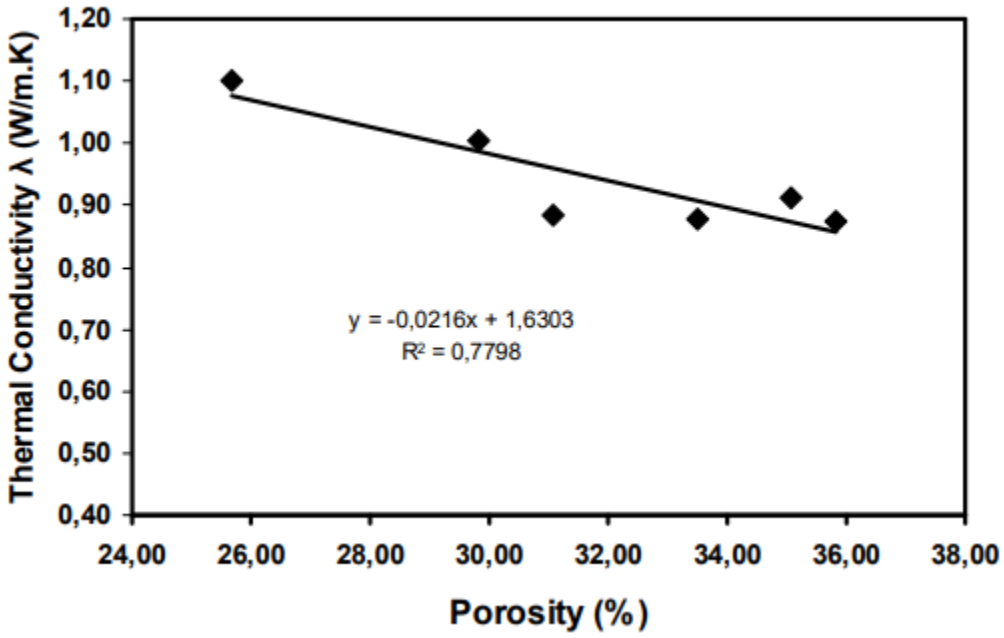

Figure 21 – Graph of porosity and thermal conductivity of dry calcarenite rock samples (Rahmouni, et al., 2013)

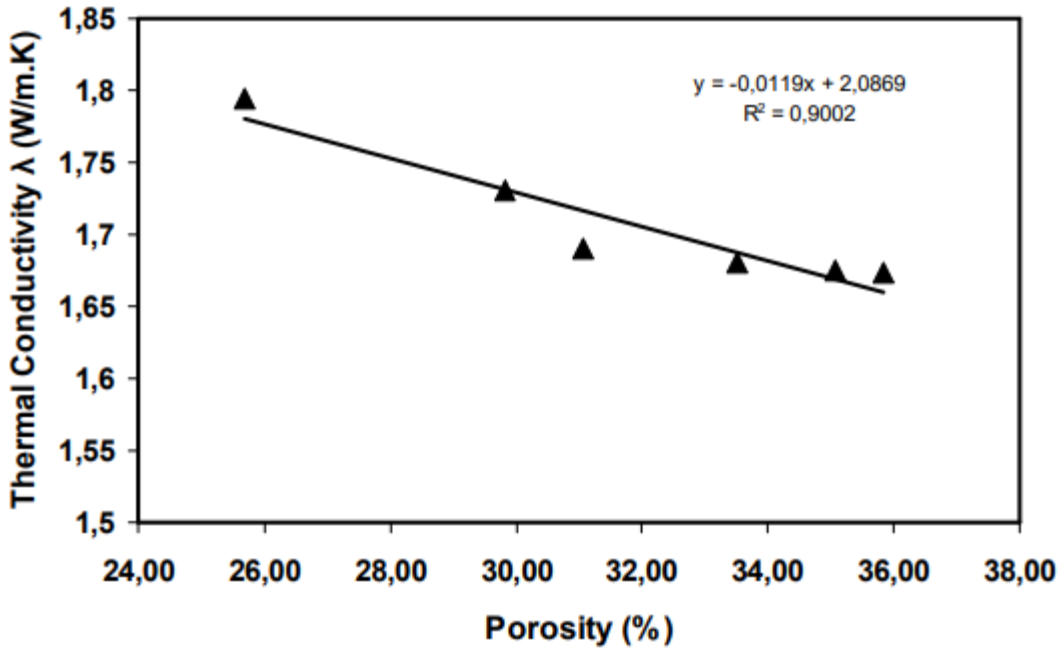

Figure 22 – Graph of porosity and thermal conductivity of saturated calcarenite rock samples (Rahmouni, et al., 2013)

4.4 Compression Test Results

The compressive strength of the nine samples was obtained by measuring the crushing load (kips) of each sample using the MTS machine and dividing that value by the cross-sectional area of the samples. These results and the calculated compressive strength are summarized below in Table 17.

Table 17 – Summary of crushing load and compressive strength of the nine samples

	1C	**2C**	**3C**	**1O**	**2O**	**3O**	**1F**	**2F**	**3F**
Crushing load (kip)	0.25	0.24	0.34	0.014	0.006	0.008	0.007	0.002	0.003
Crushing load (N)	1112	1067.52	1512.32	62.272	26.688	35.584	31.136	8.896	13.344
Diameter (mm)	25.92	26.45	26.38	25.86	25.73	25.82	26.31	26.19	26.26
Area (mm^2)	527.70	549.64	546.48	525.11	519.97	523.57	543.85	538.61	541.75
Compressive Strength (kPa)	2107.28	1942.23	2767.41	118.59	51.33	67.96	57.25	16.52	24.63

As PF is added to the samples, the compressive strength of the material significantly decreases. This agrees with other research where coconut and oil palm fibers were added in various amounts and their compressive strength was determined. Researchers Lertwattanaruk and Suntijitto used similar proportions of Portland cement, limestone powder, sand, water, and water reducer and changed the amount of natural fiber in each mix as shown in Table 18 below.

Table 18 – Summary of labels used in Figure 23

Mix	Natural Fiber (g)
OPC	0
C5	50
C10	100
C15	150
P5	50
P10	100
P15	150

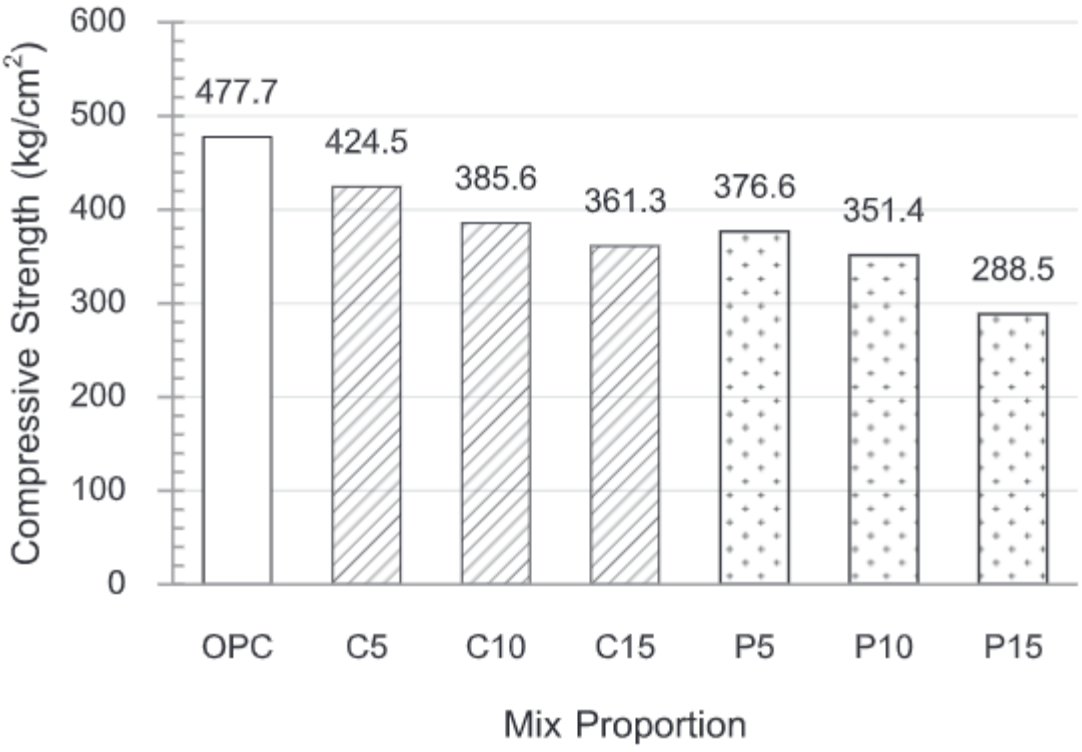

Figure 23 – Compressive strength of fiber cement mortars with various amounts of coconut or oil palm fiber (Lertwattanaruk & Suntijitt, 2015)

As both coconut and oil palm fiber were added to the mortar mixes, the compressive strength of the samples decreased from the control labeled 'OPC' shown in Figure 23. The data of this study does not match that of Lertwattanaruk & Suntijitt's research. As previously mentioned, these samples were cured following the manufacturer's, a dry cure, versus the typical wet cure most forms of industrial concrete undergo. According to the National Ready Mixed Concrete Association, concrete that is dry-cured can lose a predicted 50 percent of its potential strength and is less durable compared to wet-cured concrete. This dry curing procedure as well as the fast setting properties of the concrete mix used are the most likely culprits to the mismatched strength of this study's samples compared to existing literature. Also, the previously mentioned inconsistency in the porosity values of the samples in conjunction with the additions of PF may

have had a larger impact on the change in compression values of the samples from the control to PF modified samples.

When plotting the compressive strength of the samples against their densities in Figure 24, an overall positive trend is shown whereas density increases so does the compressive strength of the sample. This is further evidenced with the calculated correlation values of the control and 0.1% PF samples, .27 and .86, respectively. However, in the case of the 0.5% samples, there is a negative correlation value of -.61. This may be due to the interference of the porosity of these samples which were more porous than the other two groupings as previously reported in Section 4.3.

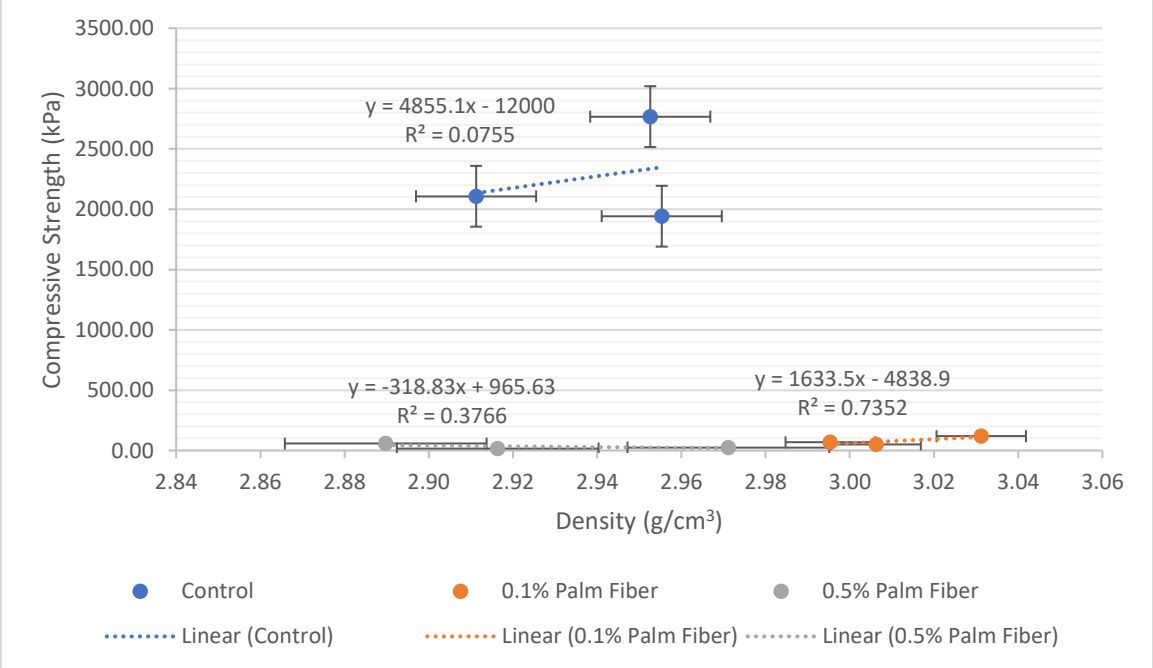

Figure 24 – Graph of density vs. compressive strength by grouping

Plotting the compressive strength versus their corresponding porosities in Figure 25 does not trend as expected. Typically, as the porosity increases the compressive strength decreases,

but instead the control and 0.5% PF samples appear to increase (Chen et al., 2013). This may be due to the inconsistent reduction of porosity by tapping the samples by hand which may interfere with how the material fails under compression.

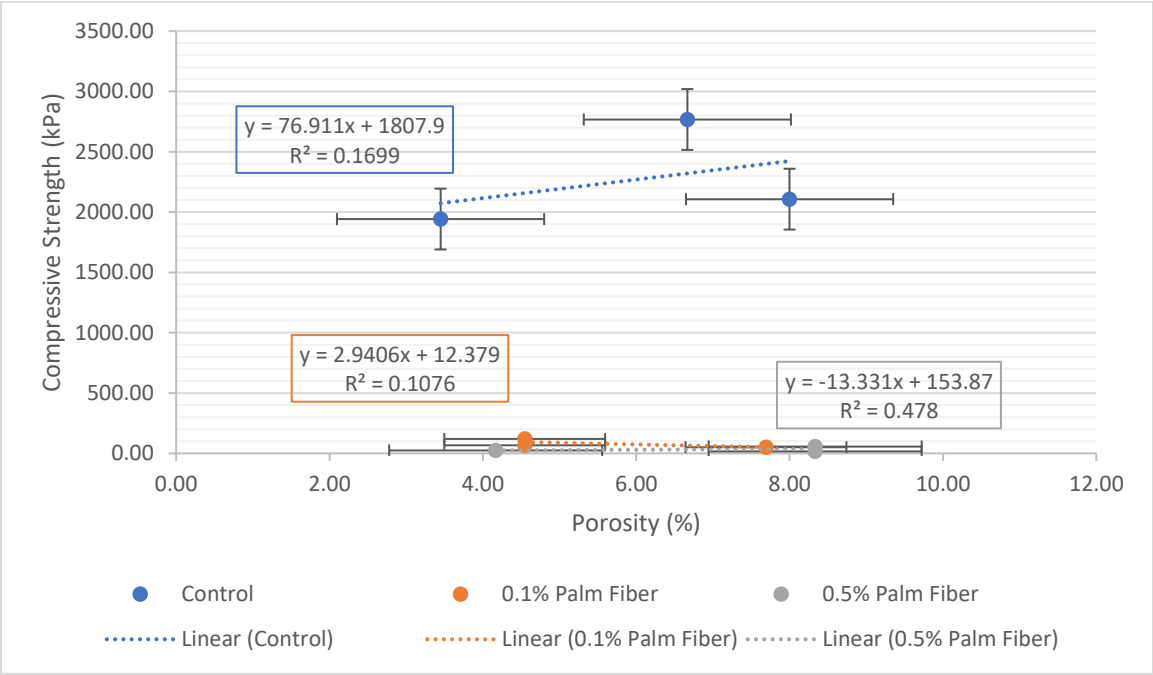

Figure 25 – Graph of porosity vs. compressive strength by grouping

A review of existing literature found no sources on the compressive strength of palm fiber. However, there is literature on the tensile strength of palm fiber, with researchers Huzaifah et al. determining an average tensile strength of 221.21±77.36 MPa (Huzaifah et al., 2017). Looking at the compressive strength of concrete, it can range from 17 MPa for residential concrete to 28 MPa for commercial structures (National Ready Mixed Concrete Association, 2014). While there is an equation to predict the compression strength of concrete from Namyong et al., the calculated result is much lower than this study's first control sample (2.11 MPa) at a predicted value of 3.63E-07 MPa. This may be because the formula was created using modeling of samples with water to cement ratios much larger than what was used in this study. The lowest

water to cement ratio in their research at 41% to this study's 11.98%. The formula detailed in Namyong et al.'s study is shown below in Equation 20 (Namyong et al., 2004).

Equation 20 – Formula to predict compressive strength of concrete mixtures (Namyong et al., 2004)

$$f_P = exp[2.393 - 1.217(w/c) - 0.0048c + 6.16\{c/(s + g)\}]$$

Where

- f_P: prediction compressive strength, MPa
- *w/c*: water-cement ratio
- *c*: cement contents, kg/m3
- *w*: water contents, kg/m3
- *c/(s+g)*: cement-aggregate ratio

4.5 Statistical Analysis Results

With the use of statistical analysis, significant differences between the control sample and the two PF samples were determined. Table 19 below shows the results of the F-test for the Control and 0.1% sample data. The order the data was applied to the F-test had to be switched as the variance of the control was higher than that of the 0.1%

Table 19 – F-Test for Control and 0.1%

F-Test Two-Sample for Variances for Control and 0.10%		
	0.10%	***Control***
Mean	10.331333	11.417
Variance	0.1179423	0.120532
Observations	3	3
Df	2	2
F	0.9785146	
P(F<=f) one-tail	0.4945703	
F Critical one-tail	0.0526315	

Because “F” is more than the “F Critical one-tail” value the null hypothesis was rejected for the control and 0.1% samples. When comparing the control and 0.5% samples, the data also needed to be switched as the variance of the control was higher than that of the 0.5% samples as shown in Table 20 below which also rejected the null hypothesis.

Table 20 – F-Test for 0.5% and Control

F-Test Two-Sample for Variances 0.5% and Control		
	0.5%	***Control***
Mean	10.33133333	11.417
Variance	0.117942333	0.120532
Observations	3	3
Df	2	2
F	0.978514696	
P(F<=f) one-tail	0.494570345	
F Critical one-tail	0.052631579	

As both F-tests established unequal variances, a t-Test was performed on both datasets with Table 21 below that shows the results of t-Test 1 on the control and 0.1% PF samples.

Table 21 – t-Test 1 results for Control and 0.1% PF samples

t-Test: Two-Sample Assuming Unequal Variances		
	Control	***0.1%***
Mean	11.417	10.33133333
Variance	0.120532	0.117942333
Observations	3	3
Hypothesized Mean Difference	0	
Df	4	
t Stat	3.850670	
P(T<=t) one-tail	0.009146	
t Critical one-tail	3.184224	
P(T<=t) two-tail	0.018292	
t Critical two-tail	3.958400	

t-Test 1 does not meet the condition of the t-stat value being more than the t-critical value, therefore the results of the modified 0.1% PF samples have do not have a statistically significant difference from that of the control samples. However, this t-Test result does not mean that there is no difference between the two data models, only that the difference is not statistically significant.

Table 22 – t-Test 2 results for Control and 0.5% PF samples

t-Test: Two-Sample Assuming Unequal Variances		
	Control	***0.5%***
Mean	16.23808	14.46939
Variance	0.073443	0.059232
Observations	3	3
Hypothesized Mean Difference	0	
Df	4	
t Stat	8.410418	
P(T<=t) one-tail	0.000547	
t Critical one-tail	3.186106	
P(T<=t) two-tail	0.001094	
t Critical two-tail	3.960548	

Unlike t-Test 1, the t-Stat value for t-Test 2 shown in Table 22 is more than the t-Critical two-tail value and the null hypothesis can be rejected, ergo the results of the 0.5% PF samples are statistically significant in their difference from the control samples.

CHAPTER V

CONCLUSIONS

Adding PF to quick set concrete reduces the thermal conductivity of quick-set concrete. While the calculated results showed a correlation of adding PF leading to a decrease in the intermediate thermal conductivity values of the samples(r= -0.8846), further statistical analysis found that there was a significant difference between the thermal conductivity of the control data and the 0.5%b PF modified samples. Replacing 0.1% of the concrete mix weight with PF yielded a decrease in thermal conductivity by 9.503% from the control sample. Replacing 0.5% with PF yields a decrease of 15.04%% from the control sample which could translate to saving as much could save as much as 369,302,1.011 kWh for the total residential consumption of energy for the state of Texas (U.S Energy Information Administration, 2019). However, this reduction in thermal conductivity comes at the cost of reduced compressive strength. Future studies should consider the addition of materials such as superplasticizers to improve the compressive strength and optimization of the thermal and physical properties.

While the usage of quick-set concrete limits the ability to extrapolate to commercial-grade concrete, this approach supplies evidence that adding organic material may produce positive results in a future study. However, to better understand the reasoning for these results, further study can be done to analyze the effects of wet and dry curing on the variation of porosity and its effect on other variables such as thermal and mechanical properties. A note for future

studies involving the H112 and H112A devices is to consider utilizing other materials such as plasticizers to improve the

compressive strength of samples and to study their effect on the thermal conductivity of the samples. As discussion over methods to reduce UHI and improve the environmental impact of new construction continues, this thesis explores a method to reduce anthropogenic heat due to the thermal conductivity of building envelope materials. While previous research has identified that improving the thermal conductivity of building materials is one possible method of reducing heat loss, there is not a robust atmosphere of analyzing the thermal properties of new or modified materials with that interest in mind. To conclude, the modifying of quick-set concrete with PF yields decreased thermal conductivity values. If this research is further expanded on in other fields of study, it can lead to a new material that can mitigate heat loss in new constructions, which can help mitigate local UHI as well as reduce their environmental impact.

REFERENCES

Abolarin, S., Gbadegesin, A., Shitta, M., Yussuff, A., Eguma, C., Ehwerhemuepha, L., & Adegbenro, O. (2013). A collective approach to reducing carbon dioxide emission: A case study of four University of Lagos Halls of residence. *Energy and Buildings, 61*, pp. 318-322.

Aboudi, J., Arnold, S. M., & Bednarcyk, B. A. (2013). Chapter 4 - The Method of Cells Micromechanics. In J. Aboudi, S. M. Arnold, & B. A. Bednarcyk, *Micromechanics of Composite Materials* (p. 176). Butterworth-Heinemann.

Agency for Toxic Substances and Disease Registry. (2004, September). *Toxic Substances Portal - Ammonia*. Retrieved September 13, 2020, from Agency for Toxic Substances and Disease Registry: https://www.atsdr.cdc.gov/phs/phs.asp?id=9&tid=2

ASTM. (2006). *Standard Test Method for Density, Absorbtion, and Voids in Hardened Concrete.* West Conshohocken: ASTM. Retrieved from ASTM International.

Becknell, N., Garver Engineers, Hale, M., Freyne, S., Durham, S., & Lamanna, A. (2006). 2006-1157: GREENCRETE: A PROJECT ON ENVIRONMENTALLY FRIENDLY CONCRETE. American Society for Engineering Education.

Benham, R., & Rehman, F. (2016). A Study of Linear Heat Transfer Gradients on 3D Printed Specimens. *Advances in Manufacturing Technology XXX: Proceedings of the 14th International Conference on Manufacturing Research, Incorporating the 31st National Conference on Manufacturing Research. 3*, pp. 137-142. IOS Press.

Bland, J., & Altman, D. (1996, June 29). Statistics notes: Measurement error. *BMJ, 312*, p. 1654.

Callister, W. D., & Rethwisch , D. G. (2007). *Materials Science and Engineering: An Introduction* (8th ed.). John Wiley and Sons.

Cellulose Insulation Manufacturers Association. (2013). *Insulation Savings Calculator*. Retrieved from Cellulose Insulation Manufacturers Association: https://cellulose.org/Cellulose-Insulation-2nd.php?pagename=CalculateSavings&dirname=HomeOwners

Chalfoun, N. (2014). Greening university campus buildings to reduce consumption and emission while fostering hands-on inquiry-based education. *Procedia Environmental Sciences*(20), 288-297.

Chen, X., Wu, S., & Zhou, J. (2013). Influence of porosity on compressive and tensile strength of cement mortar. *Construction and Building Materials, 40*, 869-874.

Clark, J. (2018, January 31). *T-Test and F-Test: Fundamentals of Test Statistics*. Retrieved from Magoosh Statistics Blog: https://magoosh.com/statistics/t-test-f-test-fundamentals-test-statistics/

de Morais, M. V., Urbina Guerrero, V. V., de Freitas, E. D., Marciotto, E. R., Valdés, H., Correa , C., . . . Vera-Puerto, I. (2019). Sensitivity of Radiative and Thermal Properties of Building Material in the Urban Atmosphere. *Sustainability, 11*(23), 6865.

Deepak Steel (India). (2020). *What do Pipe Schedules Mean?* IWS.

Demirboga, R., & Kan, A. (2012). Thermal conductivity and shrinkage properties of modified waste polystyrene. *Construction and Building Materials, 35*, 730-734.

Devore, J. L. (2011). 12.5 Correlation. In J. L. Devore, *Probability and Statistics for Engineering and the Sciences* (8th ed., pp. 508-510). Boston: Cengage Learning.

Dondi, M., Mazzanti, F., Principi, P., Raimondo, M., & Zanarini, G. (2004). Thermal Conductivity of Clay Bricks. *Journal of Materials in Civil Engineering*, 8–14.

Elfordy, S., Lucas, F., Tancret, F., Scudeller, Y., & Goudet, L. (2008). Mechanical and thermal properties of lime and hemp concrete ("hempcrete") manufactured by a projection process. *Construction and Building Materials, 22*(10), 2116-2123.

Engineering ToolBox. (2003). *Thermal Conductivity of selected Materials and Gases*. Retrieved August 22, 2020, from Engineering ToolBox: https://www.engineeringtoolbox.com/thermal-conductivity-d_429.html

Environmental Protection Agency. (2019, June 11). *Heat Island Effect*. Retrieved June 26, 2019, from EPA: www.epa.gov/heat-islands

Environmental Protection Agency. (2019). *Heat Island Impacts*. Retrieved from EPA: https://www.epa.gov/heatislands/heat-island-impacts#health

Gandage, A. S., Vinayaka Rao, V., Sivakumar, M., Vasan, A., Venu, M., & Yaswanth, A. (2013). Effect of Perlite on Thermal Conductivity of Self Compacting Concrete. *Procedia - Social and Behavioral Sciences, 104*, 187-197.

Ghrieb, A., Mitiche-Kettab, R., & Guettala, S. (2014). Relationship between Porosity, the Maximum Dry Density and. *Global Journal of Researches in Engineering: e*, 29-38.

He, B.-J. (2019). Towards the next generation of green building for urban heat islandmitigation: Zero UHI impact building. *Sustainable Cities and Society, 50*, 101647.

Helmenstine, A. M. (2020, July 1). *Random Error vs. Systematic Error*. Retrieved from ThoughtCo: https://www.thoughtco.com/random-vs-systematic-error-4175358

Huzaifah, M. R., Sapuan, M. S., Leman, Z., & Ishak, M. R. (2017). Comparative Study on Chemical Composition, Physical, Tensile, and Thermal Properties of Sugar Palm Fiber (Arenga pinnata) Obtained from Different Geographical Locations. *BioResources, 12*(4), 9366-9382.

Ishak, M. R., Leman, Z., Rahman, M. Z., Anwar, U. M., & Sapuan, S. M. (2012). Characterization of sugar palm (Arenga pinnata) fibres: Tensile and thermal properties. *Journal of Thermal Analysis and Calorimetry, 109*(2), 981-989.

Jasim, M. J., Noh, M. Z., Shihab , Z. A., Wan Ibrahim, M. H., & Takai, Z. I. (2019). Effect of Superplasticizer on Thermal Properties of Concrete. *Journal of Advanced Research in Fluid, 63*(1), 82-91.

Jawaid, M., & Khalil , A. H. (2011, April). Effect of layering pattern on the dynamic mechanical properties and thermal degradation of oil palm-jute fibers reinforced epoxy hybrid composite. *BioResources, 6*(3), 2309-2322.

Kandya, A., & Mohan, M. (2018). Mitigating the Urban Heat Island Effect through Building Envelope Modifications. *Energy and Buildings, 164*, 266-277.

Laaroussi, N., Lauriat, G., Garoum, M., Cherki, A., & Jannot, Y. (2014). Measurement of thermal properties of brick materials based on clay mixtures. *Construction and Building Materials*, 351–361.

Landwermeyer , J. S., & Rice, E. K. (1997). Comparing Quick-Set and Regular CLSM. *Concrete International, 19*(5), 34-39.

Lertwattanaruk, P., & Suntijitt, A. (2015). Properties of natural fiber cement materials containing coconut coir andoil palm fibers for residential building applications. *Construction and Building Materials, 94*, 664-669.

Magli, S., Lodi, C., Contini, F., Muscio, A., & Tartarini, P. (2015). Dynamic analysis of the heat released by tertiary buildings and the effects of urban heat island mitigation strategies. *Energy & Buildings, 114*, 164-172.

Merriam-Webster. (n.d.). *Thermal conductivity*. Retrieved December 13, 2020, from Merriam-Webster.com Dictionary: https://www.merriam-webster.com/dictionary/thermal%20conductivity

Microsoft. (2020). Microsoft Excel. Redmond, Washington, USA.

Namyong, J., Sangchun, Y., & Hongbum, C. (2004). Prediction of Compressive Strength of In-Situ. *Journal of Asian Architecture and Building Engineering, 3*(1), 9-16.

National Ready Mixed Concrete Association. (2014). Testing Compressive Strength of Concrete. *Concrete in Practice*(35).

National Ready Mixed Concrete Association. (2017). Curing In-Place Concrete. *Concrete in Practice*(11).

Nguyen, T. T., Picandet, V., Carre, P., Lecompte, T., Amziane, S., & Baley, C. (2010). Effect of compaction on mechanical and thermal. *European Journal of Environmental and Civil Engineering, 14*(5), 545-560.

Özcan, C., & Korkmaz, M. (2018). Relationship Between the Thermal Conductivity and Mechanical Properties of Uludağ Fir and Black Poplar. *BioResources, 13*(4), 8143-8154.

PA Hilton. (2019). *HEAT TRANSFER SERVICE UNIT*. Retrieved from PA Hilton: https://www.p-a-hilton.co.uk/products/heat-transfer/heat-transfer-service-unit

PA Hilton. (2019). *LINEAR HEAT CONDUCTION MODULE*. Retrieved from PA Hilton: https://www.p-a-hilton.co.uk/products/heat-transfer/linear-heat-conduction-module

Quikrete. (2020). *FAST-SETTING CONCRETE MIX*. Retrieved from Quikrete: https://www.quikrete.com/productlines/fastsettingconcretemix.asp

Rahmouni, A., Samaouali, A., Boulanouar, A., Boukalouch, M., Géraud, Y., Harnafi, M., & Sebbani, M. J. (2013). Relationship between porosity, thermal conductivity and water

saturation of calcarenites rocks. *11ème congrès de Mécanique, 2.* Agadir. Retrieved from https://www.researchgate.net/publication/261473941_Relationship_between_porosity_thermal_conductivity_and_water_saturation_of_calcarenites_rocks

Raut, A. N., & Gomez, C. P. (2016, November). Thermal and mechanical performance of oil palm fiber reinforced mortar utilizing palm oil fly ash as a complementary binder. *Construction and Building Materials, 126*, 476-483.

Safiuddin, M. D., & Hearn, N. (2005). Comparison of ASTM saturation techniques for measuring the permeable porosity of concrete. *Cement and Concrete Research, 35*(5), 1008-1013.

Sedgwick, P. (2012). Multiple significance tests: the Bonferroni correction. *BMJ, 344*(509).

Shou, L., Hayes, J., Cheng, W., Wu, C.-Y., Townshend, T., Vinson, T., & Schert, J. (2014). Characterization of ammonia gas release from concrete added with ammoniated fly ash. *Air quality, Atmosphere & Health, 7*(4), 505-513.

Streutker, D. R. (2003). Satellite-Measured Growth of the Urban Heat Island of Houston, Texas. *Remote Sensing of Environment*, 282-289.

Tannouche, A., Sbai, K., Rahmoune, M., Agounoun, R., Saadani, R., Rahmani, A., & Ounejjar, Y. (2015). An Advanced High Quality Roasting Approach of Argan Kernels Based on. *International Journal of Applied Engineering Research*, 41910-41914.

U.S Energy Information Administration. (2019). *2019 Average Monthly Bill- Residential.* Retrieved from U.S Energy Information Administration: https://www.eia.gov/electricity/sales_revenue_price/pdf/table5_a.pdf

Weisstein, E. W. (n.d.). *Bonferroni Correction*. (Wolfram) Retrieved September 15, 2020, from MathWorld: https://mathworld.wolfram.com/BonferroniCorrection.html

Wonorahardjo, S., Sutjahja, I. M., Mardiyati, Y., Andoni, H., Thomas, D., Achsani, R. A., & Steven , S. (2019). Characterising thermal behaviour of buildings and its effect on urban heat island in tropical areas. *International Journal of Energy and Environmental Engineering*, *11*, 129-142.

APPENDIX A

APPENDIX A

STATE OF THE ART SOFTWARE AND EQUIPMENT

Student Name: Monica Garcia

Thesis Title: Effect of Adding Palm Fiber to Thermal Conductivity of Quick Set Concrete

Table 23 – State-of-the-Art Equipment

Equipment	Purpose	Results Obtained
Heat Transfer Service Unit (H112)	Powers H112A Unit and measures the temperatures, voltage output, and current to be used in determining thermal conductivity	Temperatures of thermocouples, voltage output, and current needed to calculate thermal curves and thermal conductivity of tested samples
Linear Heat Conduction Module (H112A)	Heats the sample and contains thermocouples used to measure temperature values to determine thermal curves and conductivity	Temperature values needed to calculate thermal curves and thermal conductivity of tested samples
Slimline Digital Scale	Measure the mass of the tested samples	Mass of the samples used to determine density
Husky Digital 3-Mode Caliper	Measure physical properties of the samples (diameter, height)	Physical measurements used to determine cross-sectional area, bulk volume, and density
MTS Universal Testing Machine	Measure crushing load of samples	Crushing load used to determine compression strength

Table 24 – State of the Art Software

Equipment	**Purpose**	**Results Obtained**
Excel	Input raw data into worksheets, calculate thermal conductivity, plot thermal curves, and using the data analysis feature do statistical analysis	Data of the thermocouples, thermal curves over time, and statistical analysis results showing a statistically significant difference between sample groups

APPENDIX B

APPENDIX B

TEMPERATURE MEASUREMENTS (45-MINUTE TRIAL) AND CALCULATIONS FOR CONTROL SAMPLE 1

Table 25 – Temperature measurements for control sample 1, 45-minute trial

Voltage (V)	**Current (A)**	**T1 (**°C)	**T2 (**°C)	**T3 (**°C)	**T6 (**°C)	**T7 (**°C)	**T8 (**°C)
50.000	0.053	38.500	38.300	38.100	25.200	25.100	25.100
85.000	0.091	77.000	76.000	75.400	25.500	25.300	25.200
115.000	0.123	112.600	111.500	111.300	25.600	25.400	25.400

Table 26 – Temperature measurements for control sample 2, 45-minute trial

Voltage (V)	**Current (A)**	**T1 (°C)**	**T2 (°C)**	**T3 (°C)**	**T6 (°C)**	**T7 (°C)**	**T8 (°C)**
50.000	0.053	38.700	38.500	38.300	25.000	24.900	24.900
85.000	0.091	77.700	76.800	76.200	24.400	24.300	24.200
115.000	0.123	115.200	113.500	112.500	25.400	25.100	24.900

Table 27– Temperature measurements for control sample 3, 45-minute trial

Voltage (V)	**Current (A)**	**T1 (°C)**	**T2 (°C)**	**T3 (°C)**	**T6 (°C)**	**T7 (°C)**	**T8 (°C)**
50.000	0.053	38.400	38.100	37.900	24.500	24.500	24.500
85.000	0.091	76.600	75.700	75.000	24.700	24.500	24.500
115.000	0.123	113.600	112.000	110.800	24.600	24.400	24.100

Table 28 – Temperature measurements for 0.1% PF sample 1, 45-minute trial

Voltage (V)	**Current (A)**	**T1 (°C)**	**T2 (°C)**	**T3 (°C)**	**T6 (°C)**	**T7 (°C)**	**T8 (°C)**
50.000	0.053	39.000	38.700	38.400	24.900	24.800	24.800
85.000	0.091	75.000	73.900	73.300	24.900	24.700	24.500
115.000	0.123	112.400	110.700	109.400	25.900	25.400	25.100

Table 29 – Temperature measurements for 0.1% PF sample 2, 45-minute trial

Voltage (V)	Current (A)	T1 (°C)	T2 (°C)	T3 (°C)	T6 (°C)	T7 (°C)	T8 (°C)
50.000	0.053	38.600	38.200	38.100	24.400	24.400	24.400
85.000	0.091	77.200	76.200	75.600	24.500	24.300	24.200
115.000	0.123	115.200	113.500	112.400	24.600	24.400	24.100

Table 30– Temperature measurements for 0.1% PF sample 3, 45-minute trial

Voltage (V)	Current (A)	T1 (°C)	T2 (°C)	T3 (°C)	T6 (°C)	T7 (°C)	T8 (°C)
50.000	0.053	37.900	37.600	37.500	24.100	24.100	24.100
85.000	0.091	75.000	74.000	73.300	25.000	24.800	24.600
115.000	0.123	110.700	109.000	107.800	25.100	24.700	24.300

Table 31 – Temperature measurements for 0.5% PF sample 1, 45-minute trial

Voltage (V)	Current (A)	T1 (°C)	T2 (°C)	T3 (°C)	T6 (°C)	T7 (°C)	T8 (°C)
50.000	0.053	39.200	38.900	38.700	24.800	24.800	24.800
85.000	0.091	76.400	75.400	74.900	23.900	23.800	23.600
115.000	0.123	113.700	112.000	110.900	24.600	24.300	24.000

Table 32– Temperature measurements for 0.5% PF sample 2, 45-minute trial

Voltage (V)	Current (A)	T1 (°C)	T2 (°C)	T3 (°C)	T6 (°C)	T7 (°C)	T8 (°C)
50.000	0.053	38.400	38.100	37.900	23.900	23.900	23.900
85.000	0.091	76.300	75.400	74.700	24.300	24.100	23.900
115.000	0.123	112.500	110.900	109.800	24.400	24.100	23.700

Table 33 – Temperature measurements for 0.5% PF sample 3, 45-minute trial

Voltage (V)	Current (A)	T1 (°C)	T2 (°C)	T3 (°C)	T6 (°C)	T7 (°C)	T8 (°C)
50.000	0.053	37.600	37.300	37.100	23.200	23.100	23.100
85.000	0.091	73.900	72.800	72.100	23.500	23.300	23.100
115.000	0.123	109.400	107.600	106.400	24.000	23.500	23.200

Equation 21 – Calculations for control sample 1, 45-minute trial 50V

$$T_{hot\ face} = 38.1 - \frac{38.3 - 38.1}{2} = 38.0℃$$

$$T_{cold\ face} = 25.2 + \frac{25.2 - 25.1}{2} = 25.25℃$$

$$x_{int} = 33.20\ mm$$

$$k_{int(50V)} = \frac{(50V * .053A) * 33.20mm}{527.70mm^2 * (38.0 - 25.25)℃} = 13.076\frac{W}{mK}$$

Equation 22 – Calculations for control sample 1, 45-minute trial 85V

$$T_{hot\ face} = 75.4 - \frac{76.0 - 75.4}{2} = 75.1℃$$

$$T_{cold\ face} = 25.5 + \frac{25.5 - 25.3}{2} = 25.6℃$$

$$x_{int} = 33.20\ mm$$

$$k_{int(85V)} = \frac{(85V * .091A) * 33.20mm}{527.70mm^2 * (75.1 - 25.6)℃} = 9.831\frac{W}{mK}$$

Equation 23 – Calculations for control sample 1, 45-minute trial 115V

$$T_{hot\ face} = 111.3 - \frac{111.5 - 111.3}{2} = 111.2℃$$

$$T_{cold\ face} = 25.6 + \frac{25.6 - 25.4}{2} = 25.7℃$$

$$x_{int} = 33.20\ mm$$

$$k_{int(115V)} = \frac{(115V * .123A) * 33.20mm}{527.70mm^2 * (111.2 - 25.7)℃} = 10.408\frac{W}{mK}$$

Equation 24 – Intermediate thermal conductivity value of control sample 1, 45-minute trial

$$k_{int} = k_{int(50V)} + k_{int(85V)} + k_{int(115V)} = 11.105 \frac{W}{mK}$$

APPENDIX C

APPENDIX C

TEMPERATURE MEASUREMENTS (120-MINUTE TRIAL AT 50 V)

Table 34 – Temperature measurements control sample 1, 120-minute trial

Minutes	T1	T2	T3	T6	T7	T8
0	17.4	17.5	17.5	16.8	16.7	16.6
10	25.2	25.1	24.9	18.6	18.6	18.6
20	30.3	30.1	29.9	19	18.9	18.8
30	33.9	33.6	33.3	19	18.9	18.9
40	36.1	35.8	35.6	19	18.9	18.9
50	37.9	37.7	37.4	19	19	18.9
60	39.4	39	38.8	19.1	19	18.9
120	43.7	43.3	43.1	20.2	20.1	20.1

Table 35– Temperature measurements 0.1% sample 1, 120-minute trial

Minutes	T1	T2	T3	T6	T7	T8
50	36.8	36.5	36.3	19.9	19.8	19.8
60	38	37.6	37.3	19.9	19.9	19.8
70	39	38.7	38.4	19.9	19.9	19.8
80	39.9	39.5	39.3	19.9	19.8	19.8
90	40.6	40.2	39.9	19.9	19.8	19.7
100	41.1	40.8	40.5	19.9	19.9	19.9
110	41.6	41.2	40.9	19.9	19.8	19.8
120	42	41.5	41.3	19.9	19.9	19.8

Table 36– Temperature measurements 0.5% sample 1, 120-minute trial

Minutes	**T1**	**T2**	**T3**	**T6**	**T7**	**T8**
0	16	16.1	16.1	16.2	16.3	16.4
10	24.1	23.9	23.7	18.5	18.5	18.5
20	28.8	28.5	28.3	18.9	18.9	18.9
30	32.1	31.8	31.5	19.2	19.1	19.1
40	34.5	34.2	33.9	19.3	19.2	19.2
50	36.1	35.8	35.6	19.3	19.2	19.2
60	37.6	37.3	37	19.4	19.3	19.2
70	38.7	38.2	38	19.4	19.4	19.3
80	39.5	39.1	38.8	19.4	19.4	19.3
90	40.1	39.8	39.4	19.4	19.3	19.2
100	40.6	40.2	39.9	19.4	19.3	19.2
110	41.1	40.7	40.5	19.4	19.3	19.2
120	41.4	41	40.7	19.4	19.3	19.2

BIOGRAPHICAL SKETCH

Monica Garcia was born in Landstuhl, Germany in 1995. She attended Baumholder Middle High School before transferring to Sharyland Highschool and graduated in Spring 2014. She was inspired to pursue engineering after seeing various renewable technology in Germany when her father chose to work at Baumholder Army Garrison after he retired from the military. She graduated with her bachelor's degree in Mechanical Engineering in the Winter of 2018 from the University of Texas Rio Grande Valley. After consideration, she chose to pursue her master's at the University of Texas Rio Grande Valley and obtained her Master of Science in Mechanical Engineering in December 2020. Monica may be reached at garcia.monica73@yahoo.com